Journal of Nanomaterials

Biopolymer-Based Nanocomposites from Synthesis, Modelling to Advanced Applications

Lead Guest Editor: Ana C. S. Alcântara
Guest Editors: Edson C. da Silva Filho and Cesar Viseras

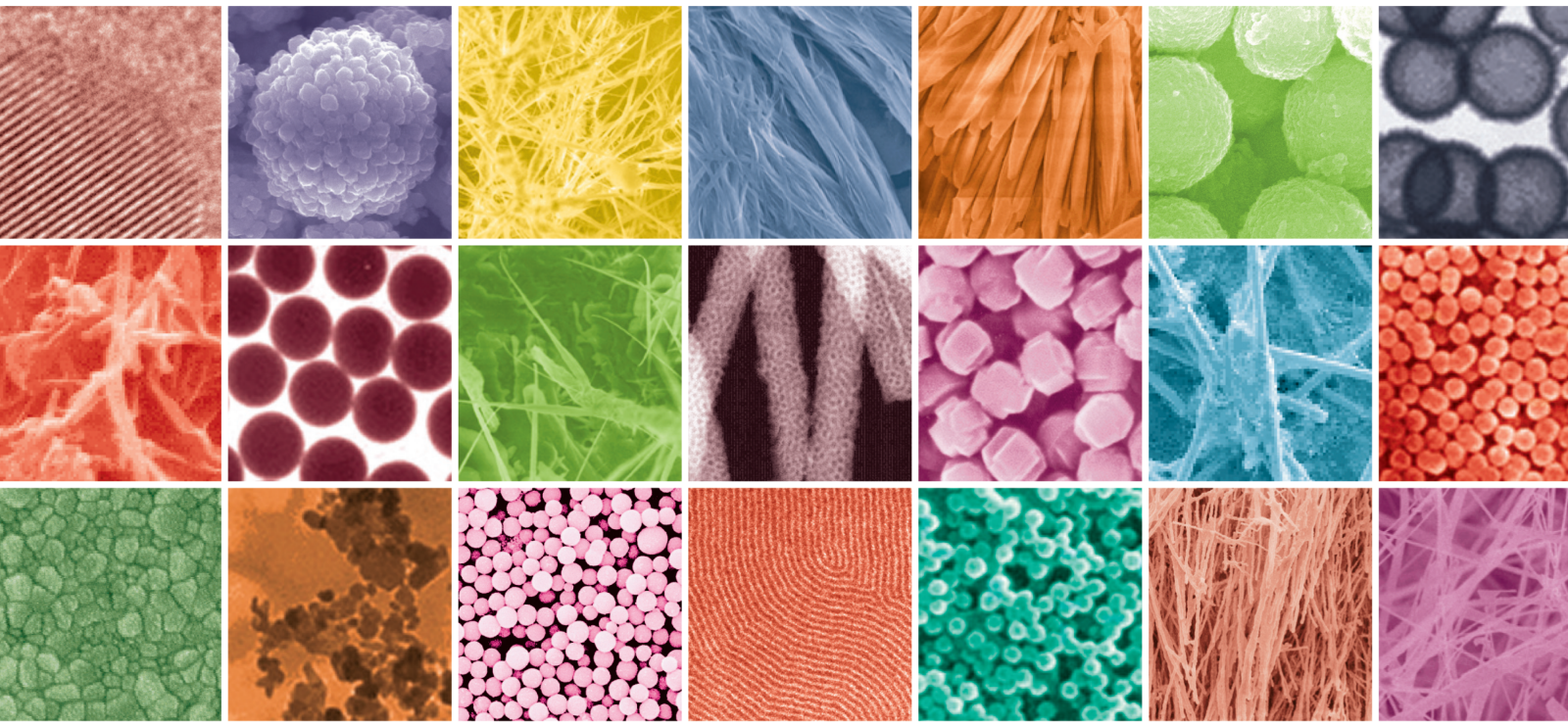

Biopolymer-Based Nanocomposites from Synthesis, Modelling to Advanced Applications

Journal of Nanomaterials

Biopolymer-Based Nanocomposites from Synthesis, Modelling to Advanced Applications

Lead Guest Editor: Ana C. S. Alcântara
Guest Editors: Edson C. da Silva Filho and Cesar Viseras

Contents

Hindawi
Journal of Nanomaterials
Volume 2020, Article ID 8040517, 16 pages
https://doi.org/10.1155/2020/8040517

Research Article

Properties of 3D Printable Poly(lactic acid)/Poly(butylene adipate-co-terephthalate) Blends and Nano Talc Composites

Wattanachai Prasong[1], **Paritat Muanchan**[1], **Akira Ishigami**[1], **Supaphorn Thumsorn**[2], **Takashi Kurose**[2] and **Hiroshi Ito**[1,2]

[1]*Graduate School of Organic Materials Science, Yamagata University, 4-3-16 Jonan, Yonezawa, Yamagata 992-8510, Japan*
[2]*Research Center for GREEN Materials and Advanced Processing (GMAP), 4-3-16 Jonan, Yonezawa, Yamagata 992-8510, Japan*

Correspondence should be addressed to Supaphorn Thumsorn; thumsorn@yz.yamagata-u.ac.jp
and Hiroshi Ito; ihiroshi@yz.yamagata-u.ac.jp

Received 25 December 2019; Revised 23 February 2020; Accepted 28 February 2020; Published 28 March 2020

Guest Editor: Ana C. S. Alcântara

Biodegradable poly(lactic acid) (PLA) filaments have been widely used in the fused deposition modeling (FDM) 3D printing technology. However, PLA has low toughness and low thermal resistance that affects printability and restricts its industrial applications. In this study, PLA was compounded with 0 to 40 wt% of poly(butylene adipate-co-terephthalate) (PBAT) and varied content of nano talc at 0 to 40 wt% in a twin screw extruder. The compounds were reextruded to filaments using a capillary rheometer. PLA/PBAT blends and their composite filaments were printed with a FDM 3D printing machine. Morphology, rheological behaviour, thermal characteristic, surface roughness, and mechanical property of 3D printing of the blends and the composites were investigated. Complex viscosity of the blends and the composites increased with increase of the PBAT and the nano talc contents. The incorporation of the nano talc enhanced crystallization temperature and reduced the coefficient of volume expansion of the composites. It was found that the PLA/PBAT blends and composites were excellent in both printability and dimension stability at PBAT content 10-30 wt% and nano talc up to 10 wt%. Interestingly, it was possible to print the composite filaments at an angle up to 75° during the overhang test without a supporter. From the vertical specimens, the surface roughness improved due to the incorporation of the nano talc. Tensile strength of the blends and the composites decreased, whereas elongation at break increased when the PBAT and the nano talc contents were increased. The reduction of tensile strength was attributed to agglomeration of the PBAT dispersed phase and less adhesion between the nano talc and the matrix. It can be noted that the composite 3D printing product showed superior elongation at break up to 410% by adding nano talc 1 wt%. This result suggests that the ductile 3D printable PLA/PBAT blend and the PLA/PBAT-nano talc composite products can be prepared, which shows potential for the commercialized scale.

1. Introduction

3D printing technology has been popular for rapid prototyping technology, which is flexible design by computer-aided design software without molds [1–9]. Up to date, the development in 3D printing technology in various applications is further required such as small parts or pseudo organs in the medical industry, new fashion clothes in the textile industry, and automotive and construction parts [2–4, 10, 11]. There are various types of 3D printing technology, which are available according to purpose and material selections. Fused deposition modeling (FDM) is widely used for polymer materials in the 3D printing technology [1–14]. Structural fabricated in FDM 3D printing is operated by extruding molten thermoplastic filament layer-by-layer deposition [5–9, 12–16]. Nevertheless, the drawbacks of 3D printing technology deal with low mechanical properties, long processing time, conflicting mass-production scale, poor dimensional stability due to thermal-induced volume shrinkage, and heat distortion of materials [2, 3]. Thus, development of 3D printing machines, software programs, 3D printable materials, and so on is still open in the FDM 3D printing technology.

The most popular thermoplastic filaments in 3D printing technology are poly(lactic acid) (PLA) and acrylonitrile-butadiene-styrene (ABS), which were derived from bio-based and petroleum-based resources, respectively [3, 4]. Owing to the global environmental problems, biodegradable and compostable plastics are becoming the key materials for the sustainable development in our future society. Therefore, material development and optimizing processability of biodegradable plastics in 3D printing, especially PLA, have been promising for various industrial fields [2–6, 12–15]. Nevertheless, PLA is known for its brittleness, low elongation at break, low impact strength, slow crystallization, and low heat distortion temperature. The incorporation of polymer blends and composites can overcome these drawbacks of PLA [17–26].

Poly(butylene adipate-co-terephthalate) (PBAT) is a biodegradable copolymer which can be degraded by microorganisms. PBAT has a superior in ductile property with high elongation at break and excellent in thermal stability [20]. PLA/PBAT blends are highly desirable materials due to high mechanical strength contributed by PLA and elevate in toughness and flexibility obtained from PBAT [18–20]. Therefore, PBAT is considered as a good candidate for enhancing the ductility of PLA [20–24]. Although PBAT is flexible and has superior toughness, it possibly loses dimensional stability during 3D printing [25]. Additionally, most 3D printing technologies require appropriate additives and fillers for controlling the printability and quality of 3D printing products [14]. The addition of fillers could reduce thermal shrinkage, warpage, and curling of the edges of conventional thermoplastic materials [3]. Talc represents one of the most useful mineral fillers for PLA, especially at high temperature service applications. Cicala et al. informed testing results of three different commercial PLA filaments for FDM [14]. The test method in this report was performed by printing a complex shape with overhang features. They found that the best printing quality is observed with the presence of mineral fillers. Zhou et al. studied the preparation of 3D printing from PBS/talc composite filaments. [27]. Several reports revealed that talc acts as the nucleating agent for PLA crystallization. The incorporation of talc increases stiffness and viscosity and improves thermal stability and heat distortion temperature of the composites, which would support dimensional stability in the 3D printing [26–30].

In this study, superior toughened biodegradable polymer blend composites from PLA, PBAT, and nano talc were prepared for alternative materials in 3D printing. Herein, a quality of 3D printable filaments was evaluated by controlled diameter of 1.70 to 1.80 mm. The effects of PBAT and nano talc contents on appearances, surface finish, and properties of dumbbell and overhang 3D printing products were investigated. Mechanical properties were performed by tensile testing. Morphology observation, rheological behaviour, thermal stability, and thermal-induced volume expansion of materials, crystallization, and thermal properties were carried out in order to clarify material characteristics during 3D printing and properties of the final 3D printed products.

Table 1: Formulations of PLA/PBAT blends and PLA/PBAT-nano talc composites.

Materials	Content (wt%)				
PLA	100	90	80	70	60
PBAT	0	10	20	30	40
Nano talc	0 to 40				

Material formulation being referred to in the abbreviations: 90/10-Talc1 = PLA 90 wt%, PBAT 10 wt%, and nano talc 1 wt%.

2. Experimental

2.1. Materials. PLA (Luminy® PLA L175) was supplied by Total Corbion PLA (Thailand) Ltd., with melt flow rate (MFR) 3 g/10 min (190°C, 2.16 kg), glass transition temperature (T_g) 55-60°C, and melting point (T_m) 175°C. PBAT (ecoflex®F Blend C1200) was provided by BASF Japan Ltd., with MFR 2.7-4.9 g/10 min (190°C, 2.16 kg) and T_m 110-120°C. Nano talc (nano ACE, D-800) was supplied by Nippon Talc Co., Ltd., Japan, in powder form, white colour, with an average particle size of 800 nm.

2.2. Preparation of PLA/PBAT Blends and PLA/PBAT-Nano Talc Composites. Materials were dried in an oven at 100°C for at least 6 h. After that, all materials with desired formulation were melted mixing by twin screw extruder (KZW15TW-30MG-NH, Technovel Co., Ltd., Japan, *L*/*D* of screw = 45). The barrel temperatures from the hopper to the die were set at 170-200°C with the screw speed of 100 rpm. The PLA/PBAT blend and the PLA/PBAT-nano talc composite were pelletized by the pelletizer. The formulations of the blends and the composites are shown in Table 1.

2.3. Preparation of 3D Printing Filaments. Pelletized PLA/PBAT blends and PLA/PBAT-nano talc composites were dried at 100°C for at least 6 h. The dried pellets were extruded into a filament by a capillary rheometer (Capilograph 10, Toyo Seiki Seisaku-sho, Ltd., Japan) at a temperature of 180°C and the extrusion speed of 40 mm/min. A circular die was used to prepare 3D printing filaments with a diameter of 1.75 ± 0.05 mm at the constant drawing speed 1.10 m/min.

2.4. Preparation of Injection Molding and 3D Printing Products. The blends and the composites were prepared as a dumbbell specimen by microinjection molding (EP5 Real Mini, Nissei Plastic Industrial Co., Ltd., Japan) at the barrel temperature from 150 to 210°C and the injection speed of 5 mm/sec.

3D printing products with different model structures were fabricated by FDM 3D printer (da Vinci 1.0 Pro, XYZprinting, Inc., Taiwan). The shape and model structures of specimens were designed and exported as standard triangle language (STL) file type in SOLIDWORKS 2017 software. Then it was exported as g-code files for cooperating the FDM printer by XYZware program as shown in Figure 1. In FDM 3D printing, there are many parameters to be

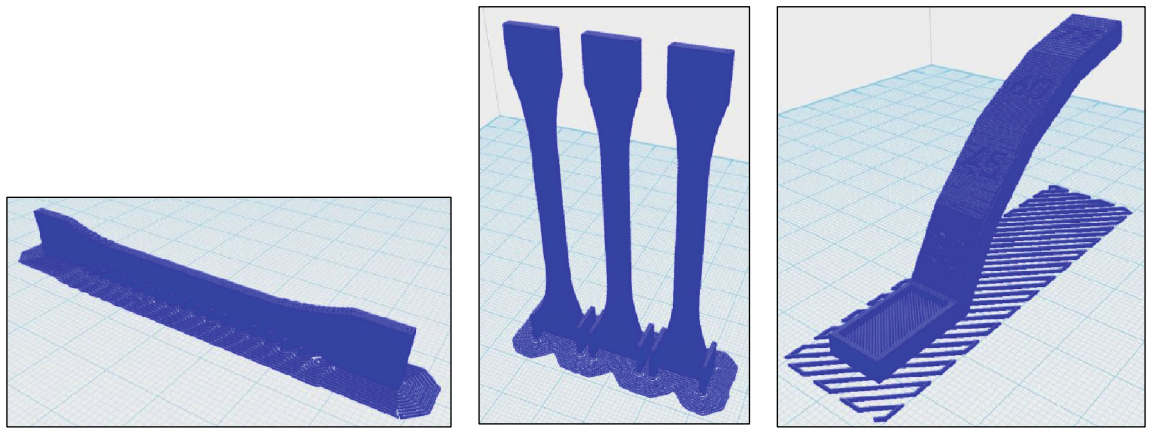

(a) (b) (c)

Figure 1: Software images of 3D printing specimens: (a) horizontal dumbbell; (b) vertical dumbbell; (c) overhang test.

Table 2: Conditions of FDM 3D printing.

Parameters	Conditions
Nozzle temperature	210°C
Bed temperature	45°C
Printing speed	25 mm/s
Infill density	100%
Infill type	Rectilinear
Layer height	0.2 mm
Shell thickness	2 layers
Filament diameter	1.75 ± 0.05 mm
Nozzle size	0.4 mm

controlled carefully such as nozzle temperature, bed temperature, printing speed, infill density, shell thickness, and layer height. In this experiment, details of the printing conditions are shown in Table 2.

2.5. Characterization

2.5.1. Morphology Observation. The samples were fractured after immersion in liquid nitrogen and then coated with platinum. Morphology of the samples was examined by scanning electron microscopy (SEM, JSM-6510, JEOL Ltd., Japan).

The inter layer of the 3D printing products was observed by SEM (TM3030plus, Hitachi, Ltd., Japan) to clarify the relationship between printing behaviour and adhesion characteristic.

2.5.2. Rheological Behaviour. Rheological behaviour of materials was measured by a rotary rheometer (Modular Compact Rheometer, MCR 302, Anton Paar GmbH, Austria). A 25 mm parallel plate was used at the frequency range of 0.01 to 1000 rad/s and the strain set at 1.0%. Complex viscosity (η^*), storage modulus (G'), and loss modulus (G'') were recorded at temperature of 210°C as a function of angular frequency (ω).

2.5.3. Pressure-Volume-Temperature Measurement. Thermal-induced volume expansion of polymers was measured by the pressure-volume-temperature (PVT) system machine (Toyo Seiki Seisaku-sho, Ltd., Japan) at temperature of 30°C to 230°C with constant pressure of 10 MPa.

2.5.4. Thermal Properties and Crystallization. Differential scanning calorimetry (DSC Q200, TA Instruments, USA) was used to analyse thermal properties and crystallization behaviour of materials. Temperature range was set at 40°C to 200°C with heating and cooling rates of 10°C/min. The sample was held isothermally for 5 min to eliminate the thermal history before cooling and the second heating [21].

2.5.5. Precision and Dimension Stability of 3D Printing Products. Precision and dimension stability of 3D printing products were evaluated by performing 3D printing dumbbell shape from vertical printing direction as shown in Figure 1(b). The overhang test specimen was performed to inspect the overhang printing quality [31]. There are 4 levels of protrusion at 30°, 45°, 60°, and 75° as presented in Figure 1(c).

2.5.6. Observation of Surface Roughness. Surface roughness of 3D printing both vertical and horizontal dumbbell specimens was measured by 3D optical surface profiler (NewView 8300, Zygo Corporation, USA) at a middle area of specimen by magnification objective 10x with scan length of 150 μm on the top field area dimension of 1,600 × 1,600 μm^2.

2.5.7. Mechanical Properties. Tensile properties of dumbbell specimen from injection molded and 3D printing products were performed according to ISO 527-2 type 1BA [32] by tensile testing machine (Strograph VG, Toyo Seiki Seisaku-sho, Ltd., Japan) at testing speed of 10 mm/min.

The notched Charpy impact test from injection molded specimen was carried out according to ISO 8256 by a digital impact tester, type DG-IB (Toyo Seiki Seisaku-sho, Ltd., Japan), at potential energy 0.1 J.

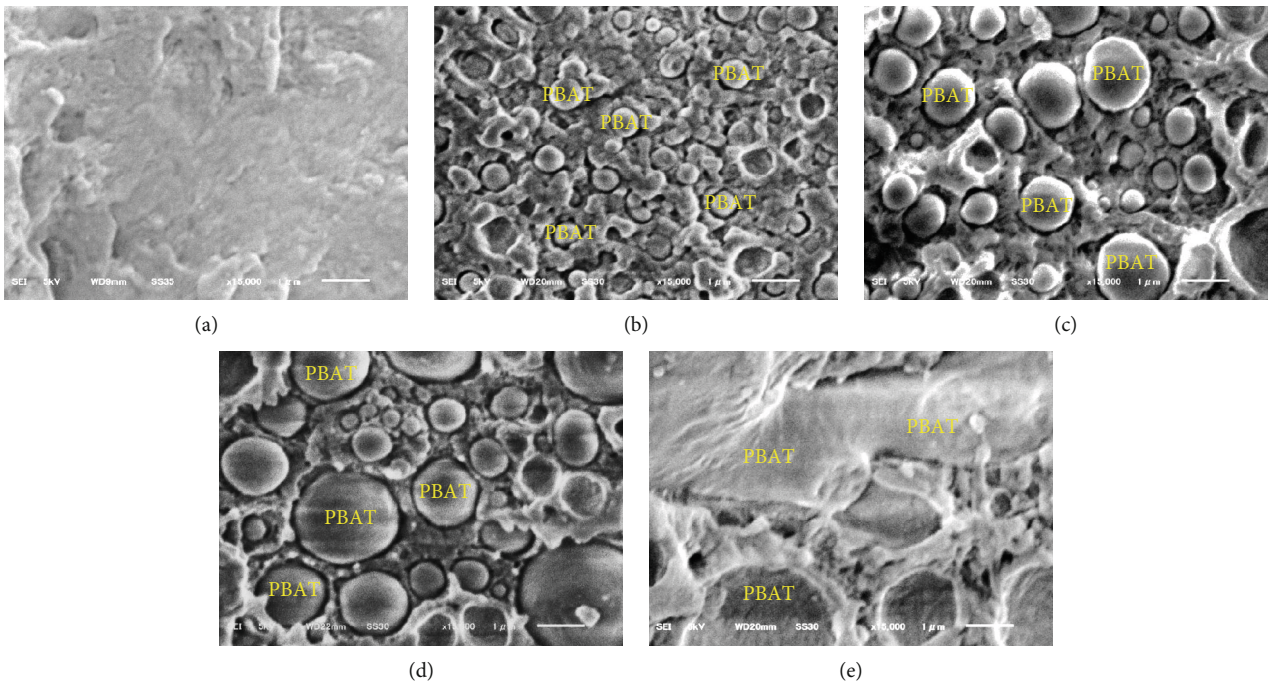

(a) (b) (c) (d) (e)

Figure 2: SEM images of cryogenic fractured surface: (a) 100/0, (b) 90/0, (c) 80/20, (d) 70/30, and (e) 60/40.

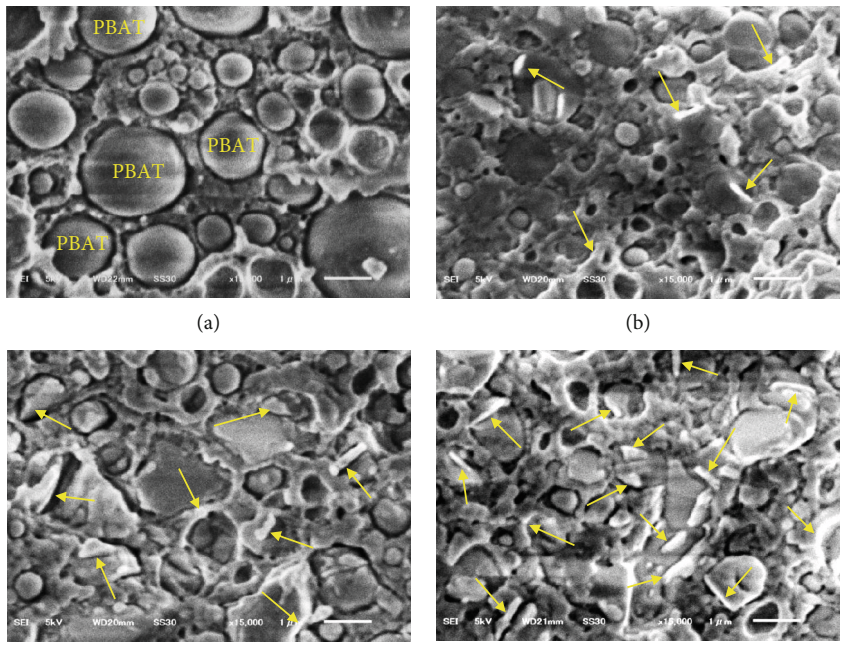

(a) (b) (c) (d)

Figure 3: SEM images of cryogenic fractured surface: (a) 70/30, (b) 70/30-talc1, (c) 70/30-talc5, and (d) 70/30-talc10.

3. Results and Discussion

3.1. Properties of PLA/PBAT Blends and Nano Talc Composites

3.1.1. Morphology of PLA/PBAT Blends and Composites. Morphology of PLA/PBAT blends and 70/30-nano talc composites is shown in Figures 2 and 3, respectively. Figures 2(a)–2(e) present the fractured surface of the PLA/-PBAT blends at PBAT contents 0-40 wt%. It can be seen that PBAT particles were dispersed on the PLA matrix, which indicated that PLA/PBAT was immiscible [33]. The PBAT dispersed phase sizes were in the range of 0.6-1.2 μm, which they became larger when increasing the PBAT contents [33–36]. However, the dispersed phase exhibited cocontinuity

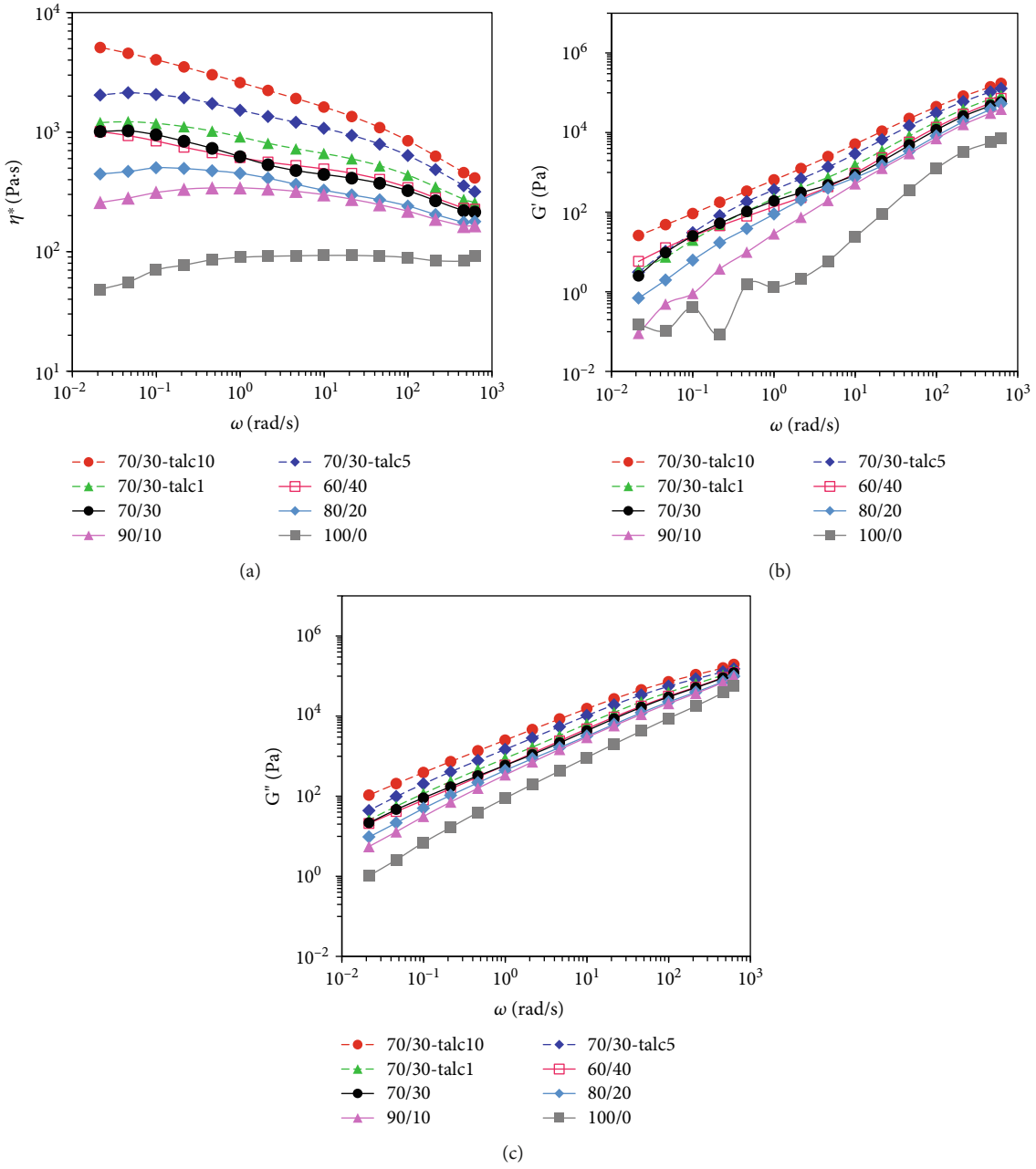

Figure 4: Rheological properties of PLA/PBAT blends and 70/30-nano talc composites: (a) complex viscosity (η^*), (b) storage modulus (G'), and (c) loss modulus (G'').

structures at the content of PBAT 40 wt% as shown in Figure 2(e), which was due to the coalescence of PBAT [33, 34]. Figures 3(a)–3(d) depict the morphology of the 70/30-nano talc composites at the nano talc content 0-10 wt%. It was found that nano talc particles, indicated by arrows in the SEM images, were distributed well on the polymer blend matrix [33]. The PBAT dispersed phase size in the composites became smaller as compared to the 70/30 blend. It was considered that the nano talc particles hindered an agglomeration of PBAT because of an increment of polymer viscosity and surface tension. Hence, the nano talc particles delay the mass transfer during the coalescence of PBAT [33–35].

3.1.2. Rheological Behaviour of PLA/PBAT Blends and Nano Talc Composites. Rheological properties of the blends and the composites are carried out for 3D printing technology in order to determine the printability, dimension stability, and interlayer adhesion in the 3D printing process [7, 18, 27]. Figure 4 illustrates complex viscosity (η^*), storage modulus (G'), and loss modulus (G'') from viscoelastic behaviour of the PLA/PBAT blends and the 70/30-nano talc composites. The complex viscosity as a function of frequency of the PLA/PBAT blends and the composites exhibited pseudoplastic (shear thinning), whereas neat PLA exhibited Newtonian behaviour at higher frequency [18, 27]. The complex viscosity of the blends increased when increasing the

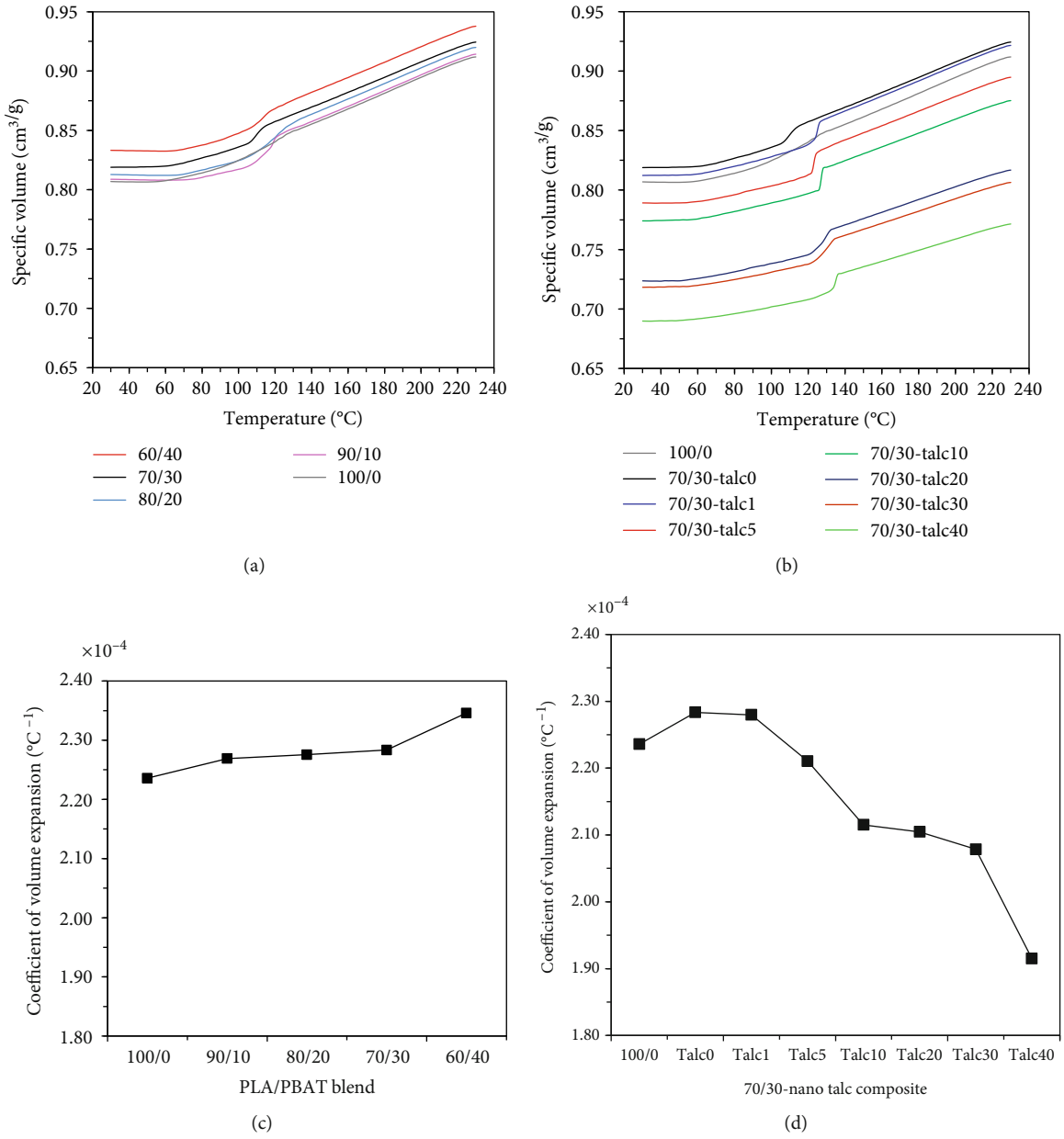

Figure 5: Specific volumes of the (a) PLA/PBAT blend and (b) 70/30-nano talc composite and the coefficients of volume expansion of the (c) PLA/PBAT blend and (d) 70/30-nano talc composite.

PBAT and the nano talc contents as shown in Figure 4(a). Storage modulus and loss modulus of the blends and the composites were also higher than neat PLA as presented in Figure 4(b) and 4(c). It was considered that PBAT has long and flexible molecular chains resulting in elastic deformation due to molecular entanglement [5, 22]. In addition, nano talc inhibited the movement of the polymer chains, which induced stiffness and solid like of molten polymer, especially at low frequency [14, 27, 37–39]. An increment of the storage modulus of the composites informed fine distribution of nano talc and the interaction between nano talc and polymer matrix [5]. Additionally, from Figure 4(b) at low frequency, small plateau of the storage modulus of 70/30 and 60/40 blends indicated changing of elasticity to rubbery flow due to highly entanglement during relaxation process at low frequency [38]. The declination of the complex viscosity and the sudden drop of the storage modulus in neat PLA might be due to deterioration of PLA chain at testing temperature (210°C) [6]. The degree of the complex viscosity would inform printing characteristic. Cicala et al. reported that low viscosity and elasticity of material resulted in flow and dripping of layer deposition that was fallen as poor printing quality [14]. On the contrary, polymers with high viscosities are difficult in printing and lead to inconsistent flow from the nozzle [7]. Qahtani et al. found that their printing job failed due to high viscosity and dimensional instability [6]. Hence,

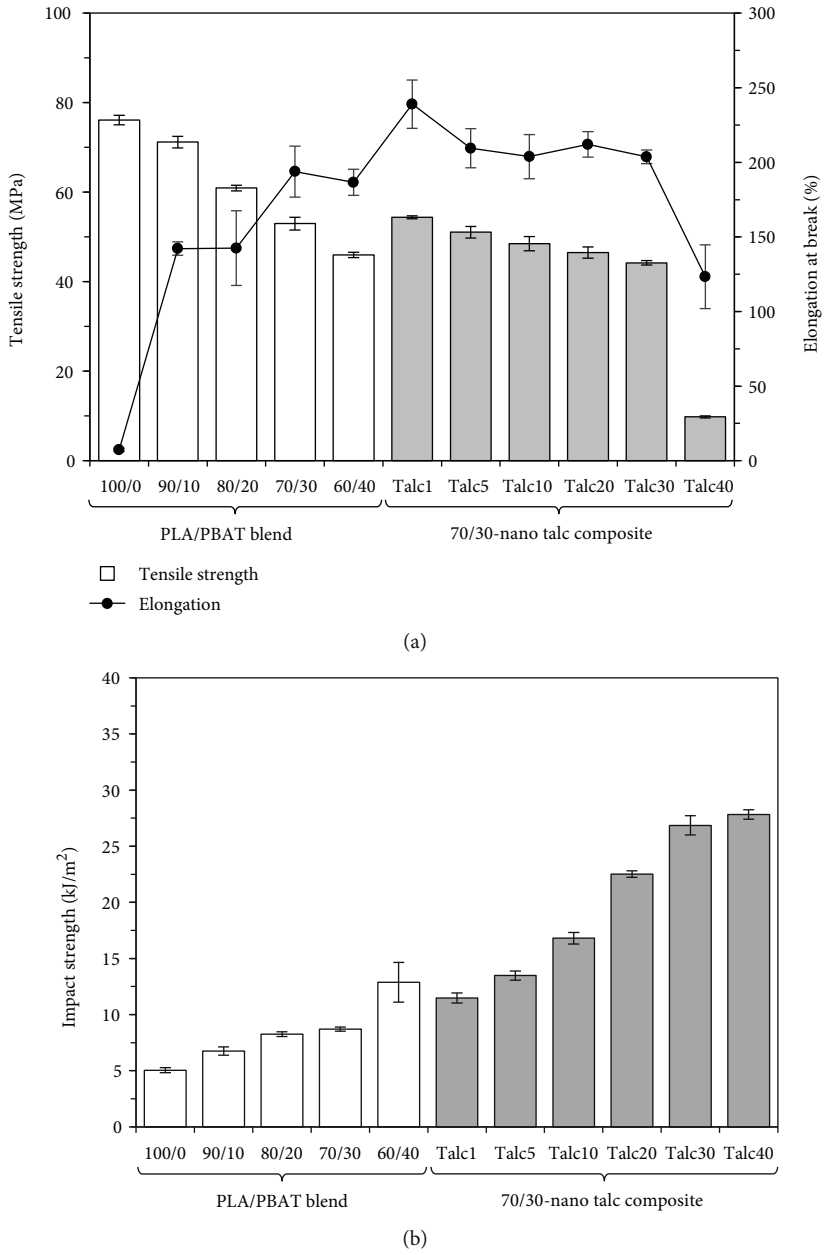

Figure 6: Mechanical properties of PLA/PBAT blends and 70/30-nano talc composites: (a) tensile strength and elongation at break; (b) impact strength.

polymer filament viscosity must be moderate to achieve successful FDM processing conditions [6]. Therefore, the effect of the PBAT and the nano talc contents on the rheological behaviour of the blends and the composites would explain dimension stability of their 3D printing products.

3.1.3. Specific Volume and Coefficient of Volume Expansion. The specific volume of the PLA/PBAT blends and the composites was analysed by PVT measurement at constant pressure with variations of temperatures. Results of the PVT measurement, i.e., the specific volume and the coefficient of volume expansion, are presented in Figure 5. The specific volumes of the blends and the composites rose at elevated temperature as shown in Figures 5(a) and 5(b). The value of the specific volume increased with the incorporation of PBAT as shown in Figure 5(a), which was due to the increment of polymer chains mobility. On the contrary, the addition of nano talc decreased the value of specific volume in the composites, and the value drastically dropped at higher contents of nano talc from 5 wt% to 40 wt% as presented in Figure 5(b). The results indicated that the nano talc restricted polymer chain mobility in the 70/30-nano talc composites during the elevated temperature.

The coefficient of linear thermal expansion (CLTE) and the coefficient of volume expansion can be used for determining dimension changes through printability in the 3D

Table 3: Mechanical properties of PLA/PBAT blends and 70/30-nano talc composites.

PLA/PBAT-nano talc	Tensile strength (MPa)	Young's modulus (GPa)	Elongation at break (%)	Impact strength (kJ/m^2)
100/0-talc0	76.1 ± 2.80	2.3 ± 0.14	7.3 ± 3.30	5.0 ± 0.60
90/10-talc0	71.2 ± 3.10	2.2 ± 0.95	142.2 ± 12.50	6.8 ± 1.09
80/20-talc0	60.9 ± 1.50	2.3 ± 0.06	142.5 ± 54.50	8.2 ± 0.46
70/30-talc0	53.0 ± 3.60	2.0 ± 0.20	193.8 ± 49.60	8.7 ± 0.49
60/40-talc0	46.0 ± 1.70	1.8 ± 0.20	186.6 ± 23.17	12.9 ± 3.86
70/30-talc1	54.4 ± 1.00	2.2 ± 0.30	239.0 ± 45.30	11.5 ± 1.09
70/30-talc5	51.0 ± 3.30	2.2 ± 0.17	209.4 ± 32.20	13.5 ± 1.01
70/30-talc10	48.5 ± 4.38	2.1 ± 0.17	203.9 ± 38.65	16.8 ± 1.25
70/30-talc20	46.5 ± 3.00	2.4 ± 0.17	212.0 ± 20.10	22.5 ± 0.95
70/30-talc30	44.2 ± 1.45	2.6 ± 0.40	203.7 ± 11.10	26.8 ± 2.17
70/30-talc40	9.8 ± 0.06	3.1 ± 0.34	123.3 ± 64.40	27.8 ± 1.17

printing technology [3, 6, 40]. In this research, the coefficient of volume expansion (β) can be estimated from the specific volume as the following equation [40]:

$$\beta = \frac{1}{V}\left(\frac{\Delta V}{\Delta T}\right), \quad (1)$$

where V is a specific volume at room temperature, ΔV is a change in the specific volume due to heating or cooling, and ΔT is temperature differences in the range of the change in the specific volume.

Figures 5(c) and 5(d) display the coefficient of volume expansion of the PLA/PBAT blends and the composites, respectively. The coefficient of volume expansion of the blends increased when increasing the content of PBAT as presented in Figure 5(c). It was considered that PBAT is a long molecule chain that was easily moved during thermal induction, which resulted in higher values of the coefficient of volume expansion [41]. It can be implied that the materials having high thermal-induced volume expansion may dominate thermal instability of molten filament resulting in poor dimension stability, warpage, and shrinkage in the 3D printing products [3, 6]. On the other hand, the coefficient of volume expansion of the composites decreased when increasing the nano talc content as depicted in Figure 5(d). It was due to superior thermal resistance of the nano talc that prevented the expansion of the composites during the elevated temperature [42, 43]. It has been reported that the addition of mineral fillers in 3D printing filaments decreased the coefficient of volume expansion, which contribute for improving printability, reducing warpage, shrinkage, and printing defects in the 3D printing process [3].

3.1.4. Mechanical Properties of Injection Molded Parts. The effects of the PBAT and the nano talc contents on mechanical properties of injection molded parts have been investigated in order to clarify the ratio between the PLA/PBAT blends and the nano talc contents for the 3D printing process. Figure 6 and Table 3 show tensile and impact properties of the PLA/PBAT blends and the composites.

From Figure 6(a) and Table 3, tensile strength and Young's modulus of the PLA/PBAT blends decreased while elongation at break increased when increasing the PBAT content. The declination of tensile strength and Young's modulus and the increment of elongation at break were attributed to high ductility, low modulus, and low tensile strength of PBAT [34, 38]. The maximum elongation at break of 193.8% was found at the 70/30 blend. However, the reduction of the elongation at break in the 60/40 blend might due to larger dispersed phase sizes as well as the cocontinuity structured in the 60/40 PLA/PBAT blend as presented in Figure 2 [34]. From the results, the 70/30 blend was selected to composite with the nano talc.

The effect of the nano talc on mechanical properties of the 70/30-nano talc composites has been discussed. Young's modulus significantly increased with increasing the nano talc contents from 20 wt% to 40 wt% as depicted in Figure 6(a) and Table 3, which was due to the stiffness of the nano talc. At the content of the nano talc 1 wt% to 30 wt%, tensile strength in the composites was lower, whereas elongation at break of the composites was higher than the 70/30 blend. These results were attributed to the less adhesion between the nano talc and the polymer blend matrix and the reduction of PBAT dispersed phase when adding the nano talc in the composites as shown in Figure 3. It is interesting to note that the maximum elongation at break about 239% was observed at the composite with 1 wt% of nano talc. However, the values of both tensile strength and elongation at break were greatly reduced at 40 wt% of nano talc. It was considered that nano talc was highly agglomerated and restricted the movement of polymer chain in the composites and the macro phase separation between the filler and the matrix [44, 45]. The results suggested that the maximum of the nano talc content in the PLA/PBAT composite should be less than 30 wt% for optimizing material properties.

Figure 6(b) depicts the impact strength of the PLA/PBAT blends and the composites. From the result, the impact strength of the blends and the composites increased with increasing the contents of PBAT and nano talc. It was due to the ductility of PBAT and the reduction of PBAT dispersed phases in the blends and the composite [33, 45]. Therefore,

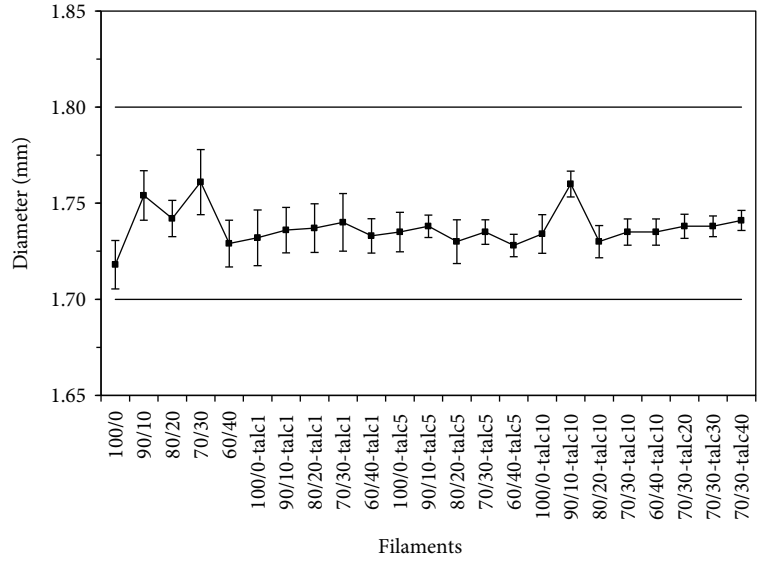

Figure 7: Diameter of 3D printing filaments.

the PLA/PBAT blends and the nano talc composites were able to absorb more energy and performed higher values of the impact strength as compared with neat PLA.

3.2. Production of 3D Printing Filaments. The 3D printing filaments of the PLA/PBAT blends and the nano talc composites were successfully prepared by capillary rheometer (vertical extrusion). The diameter of all filaments can be controlled in the range of 1.75 ± 0.05 mm as shown in Figure 7. The deviation of the diameter was reduced when increasing the nano talc content, which was considered from the increasing in the viscosity and the decreasing of the coefficient of volume expansion in the composites. Therefore, high viscosity and low values of the coefficient of volume expansion were benefits for preparation and control filament diameters especially in the vertical flow of capillary rheometer.

3.3. Properties of 3D Printing Products

3.3.1. Dimension Stability and Printability of the 3D Printing Products. In this study, the PLA/PBAT blends and the 70/30-nano talc composites were neatly printed in the horizontal dumbbell specimen. Hence, the printability and the dimension stability of the 3D printing products were evaluated from the vertical dumbbell and the overhang test specimens as presented in Figures 8 and 9, respectively. From Figure 8, the PLA/PBAT blends can be maintained the shape up to 20 wt% of the PBAT content. The rough surface appeared in the 70/30 blend specimen, and the printing was not completed at the 60/40 blend. It was attributed to the flexibility of PBAT and the high value of the coefficient of volume expansion at printing temperature. Therefore, these specimens exhibited lack of consistency and less dimension accuracy in the printing products. On the contrary, the addition of the nano talc significantly improved the printing of the PLA/PBAT blend composite, especially the 60/40 blend as shown in the bottom line of Figure 8. Cicala et al. reported that mineral fillers act as reinforcement in printed parts that kept their shape during printing [14]. In addition, Figure 9 shows the effect of the nano talc contents on the overhang test products in the 70/30-nano talc composites. The results revealed that the dimension stability of the 3D printing products of the 70/30 composite was successfully improved when increasing the nano talc content. It can be noted that the composite printing products were possible to be produced even in the angle up to 75° for the overhang test without a supporter, which is better than a conventional standard at 45° of design rules for the FDM 3D printing [14, 31]. The incorporation of the nano talc in the 70/30 blend depicted the improvement of dimension stability as well as surface characteristic. It was due to the reinforcement of the nano talc, the increment of the viscosity, and the reduction of the coefficient of volume expansion in order to control the stability of the molten filament [3, 6, 14, 27].

3.3.2. Thermal Properties and Crystallization Behaviour of the 3D Printing Products. Figure 10 illustrates DSC thermograms of the PLA/PBAT blends and the 70/30-nano talc composites at the nano talc content 1-10 wt%. Results of glass transition temperature (T_g), cold crystallization temperature (T_{cc}), melting temperature (T_m), crystallization temperature (T_c), enthalpy of cold crystallization (ΔH_{cc}), enthalpy of melting (ΔH_m), and degree of crystallinity (X_c) of the 3D printing products from the cooling cycle and the second heating are tabulated in Table 4. The degree of crystallinity was calculated based on the following equation [17, 18]:

$$X_c\,(\%) = \frac{\Delta H_m - \Delta H_{cc}}{\Delta H_f^0} \times \frac{1}{W} \times 100, \quad (2)$$

where ΔH_m is the enthalpy of melting, ΔH_{cc} is the enthalpy of cold crystallization, $\Delta H^0{}_f$ is the heat of fusion for fully crystalline PLA 93.7 J/g [18], and W is the weight fraction of PLA in the PLA/PBAT blends and the composites.

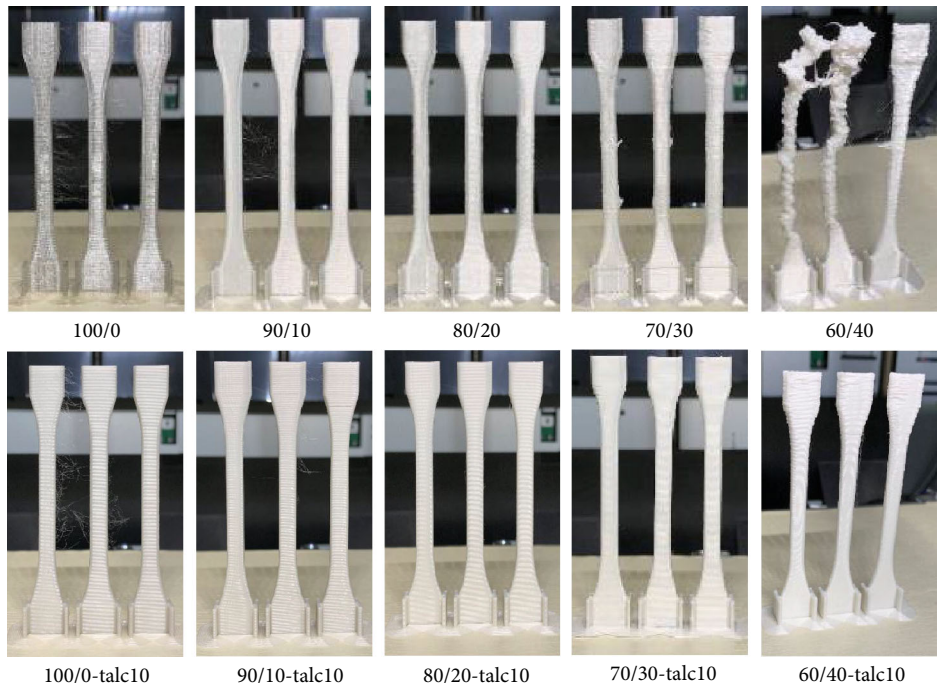

Figure 8: Photographs of vertical dumbbell 3D printing specimens.

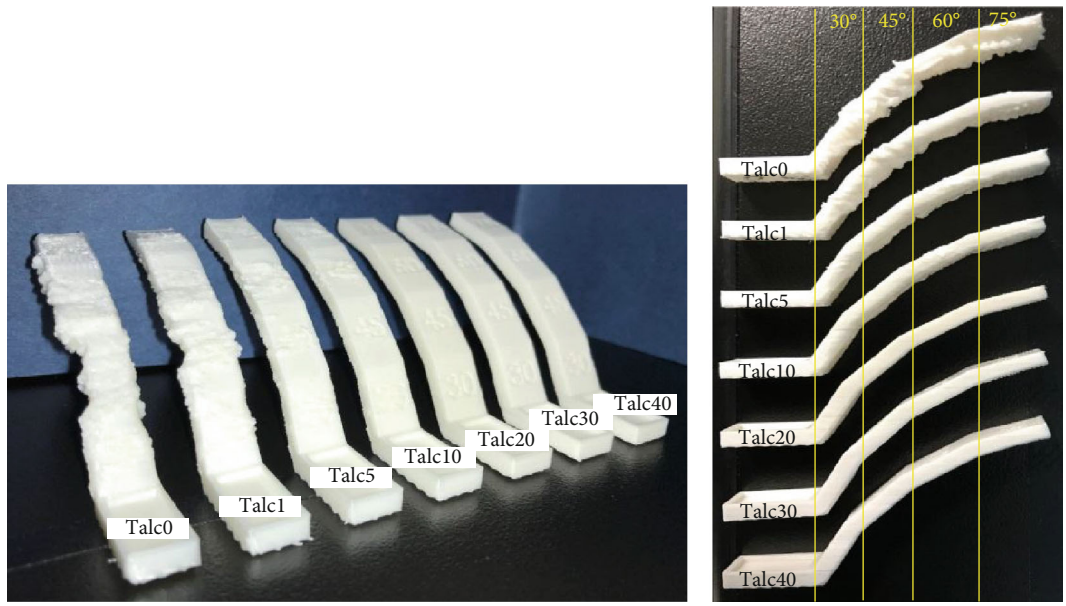

Figure 9: Overhang test specimens of 70/30-nano talc composites.

Figures 10(a) and 10(b) depict DSC thermograms from the first heating of the PLA/PBAT blends and the composites, respectively. The cold crystallization in the blends and the composites can be observed, which indicated that the polymer chain does not have enough time for organizing and ordering polymer molecules to crystallize during printing products. However, the addition of the nano talc decreased the cold crystallization temperature in the 70/30-nano talc composites in which the nano talc promoted the crystallization in the composites. The results were confirmed by sharper of the crystallization temperature in the composites as compared to the PLA/PBAT blends as shown in the cooling cycle in Figures 10(c) and 10(d). Furthermore, the cold crystallization existed in the blends while it disappeared in the composites in the second heating as depicted in Figures 10(e) and 10(f), respectively.

Table 4 summarizes thermal properties of the blends and the composites from the cooling cycle and the second

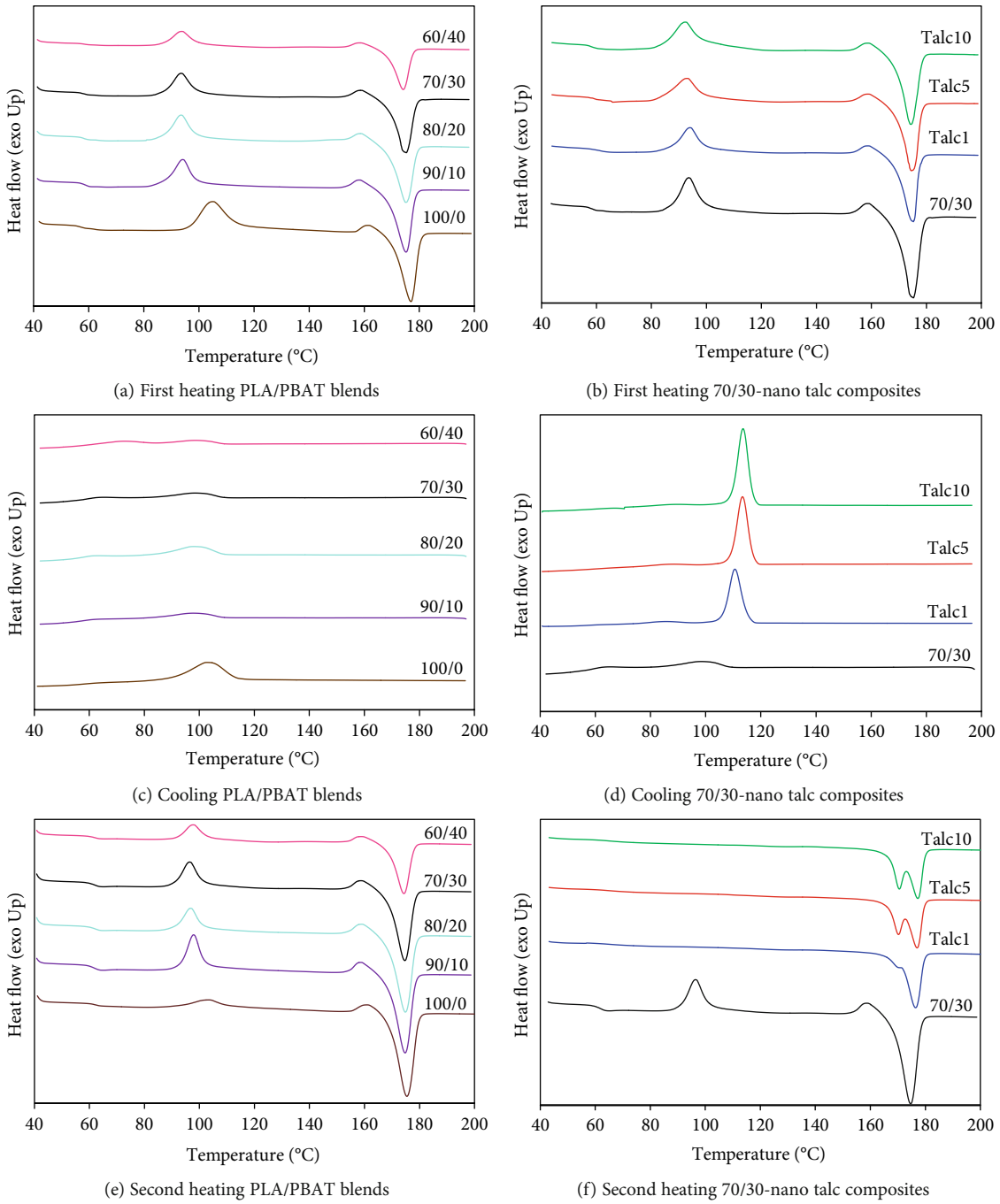

(a) First heating PLA/PBAT blends

(b) First heating 70/30-nano talc composites

(c) Cooling PLA/PBAT blends

(d) Cooling 70/30-nano talc composites

(e) Second heating PLA/PBAT blends

(f) Second heating 70/30-nano talc composites

Figure 10: DSC thermograms of 3D printing specimens.

heating. The crystallization temperature of PLA in the blends was low in which PBAT retarded the crystallization of PLA during printing. On the other hand, the incorporation of the nano talc increased crystallization temperature of PLA in the composites, and the cold crystallization was vanished in the composites. The results implied that the nano talc improved the PLA crystallization in the 70/30-nano talc composites, which confirmed by higher degree of crystallinity of PLA in the composites than in the blends. It was considered that the nano talc acted as the heterogeneous nucleation site while PBAT dispersed phase retarded for PLA to crystallize [44–49]. Double peaks of the melting endotherm in the composites after printing as presented in Figure 10(d) indicated partial melting, recrystallization, and remelting of crystal in the composites [38, 45, 49]. The increment of the glass transition temperature of PLA in the composites informed the restriction of polymer chain mobility because of the addition of the nano talc. It can be noted that the increasing of the crystallization temperature and the glass transition temperature of PLA in the composites notified faster solidification of molten polymer and reinforcing of the printing products, respectively.

Table 4: Thermal properties of PLA/PBAT blends and composites.

PLA/PBAT-nano talc	T_c (°C)	T_g (°C)	T_{cc} (°C)	ΔH_{cc} (J/g)	PLA $T_{m\,peak1}$ (°C)	PLA $T_{m\,peak2}$ (°C)	ΔH_m (J/g)	X_c (%)
100/0	102.6	60.0	103.4	11.2	—	175.4	46.6	37.8
90/10	97.5	59.3	97.6	24.0	—	174.7	41.2	20.4
80/20	98.0	59.7	96.8	16.0	—	174.8	35.1	25.5
70/30	98.6	59.7	96.4	17.0	—	174.7	30.8	21.0
60/40	99.1	59.6	97.8	13.4	—	174.2	26.4	23.1
70/30-talc1	110.5	62.5	—	—	—	176.4	32.1	49.5
70/30-talc5	113.3	63.1	—	—	170.2	176.9	31.2	49.9
70/30-talc10	113.6	64.3	—	—	170.6	177.3	29.3	49.2
70/30-talc20	114.6	61.2	—	—	170.0	176.7	29.4	53.7
70/30-talc30	114.7	61.9	—	—	170.2	176.6	27.4	54.3
70/30-talc40	115.6	60.1	—	—	170.4	176.7	26.2	56.0

3.3.3. Surface Roughness of the 3D Printing Products. Figure S1 presents the scanning profile of the surface roughness measurement. The 3D surface roughness data was evaluated as the surface roughness average (R_a) by Zygo Mx software according to Equation S1 [50]. Surface roughness average (R_a) of the vertical and the horizontal dumbbell specimens is presented in Figures 11(a) and 11(b) for the PLA/PBAT blends and the 70/30-nano talc composites, respectively. At the vertical printing direction, the surface roughness significantly increased when increasing the PBAT content in the blends while drastically decreased with the addition of the nano talc in the 70/30-nano talc composites. According to the PLA/PBAT blends, the volume of molten polymer in the blends increased at the printing condition as observed from high values of the coefficient of volume expansion in the blends. Therefore, the molten filament was instability, and the printed layers of the blends have less time to solidify completely before the next printing level resulted in surfaced defect in the vertical specimen [2, 50, 51]. At the horizontal printing direction, the surface roughness of the blends and the composites was lower than the neat PLA and the PLA commercial filament ($R_a = 20.7\,\mu$m). The surface roughness decreased when increasing the content of PBAT in Figure 11(a), whereas it almost unchanged when adding the nano talc in Figure 11(b). It was considered that the melted layers have time for adhered and solidified layer by layer in the horizontal printing direction. Hence, the surfaces of the horizontal specimens were smooth. It can be noted that the PBAT and the nano talc improved the dimensional accuracy and the surface quality of these horizontal specimens [50, 51].

3.3.4. Adhesion between Interlayers. Since molten polymer is fabricated layer by layer in 3D printing, an integrity of adhesion between the layers is required in order to enhance mechanical properties of 3D printing products [6]. The bonding between layers of FDM parts is driven by the thermal energy of the semimolten material [9]. Figure S2 shows the schematic observation of interlayer and voids from cross-sectional vertical dumbbell specimen. Figures S3 and S4 present SEM images of alignment layers in the PLA/PBAT blends and the 70/30-nano talc composites, respectively. Figure 12 depicts SEM images of the interlayers in the PLA/PBAT blends and the 70/30-nano talc composites at high magnification. Voids, which are indicated by arrows, can be observed between layers in neat PLA, the blends and the composites. Sizes of the voids obviously decreased with adding higher contents of PBAT as shown in Figures 12(a)–12(c), which provides larger contact area in the blends [8]. On the contrary, the sizes of the voids increased when increasing the nano talc contents as presented in Figures 12(d)–12(f). The result was considered that the reduction of the voids was due to higher values of the coefficient of volume expansion of PLA/PBAT blends. Thus, the melted layers were easily adhered during printing and continuing immersed layer by layer when increasing the PBAT contents. On the other hand, the voids between layers increased with increasing the nano talc contents. Since the adding of nano talc increased the viscosity, reduced the coefficient of volume expansion, and enhanced the crystallization temperature of the composites, the diffusion of polymer molecular chain was retarded, and between layers were solidified faster resulting in the reduction of filaments welding, which exhibited larger voids and lack of interlayer adhesion [3, 8, 14, 50].

3.3.5. Tensile Properties of the 3D Printing Products. Tensile properties of the 3D printed dumbbell specimens are shown in Table 5. Tensile strength of the blends and the composites decreased in both of horizontal and vertical dumbbell specimens with increasing the PBAT and the nano talc contents. It was owing to the ductility of the PBAT and less adhesion between the nano talc and the polymer matrix. The elongation at break of the blends and the composites increased when increasing the contents of PBAT and nano talc, which was accounted to the reduction of PBAT dispersed phase sizes and the orientation of printed layer in the horizontal specimens. However, the elongation at break of the composites with horizontal printing decreased at high nano talc contents because of the cluster of the nano talc in the composites. On the contrary, the blends and the composites at the vertical printing direction were difficult to elongate because of poor adhesion between the printed layers, which

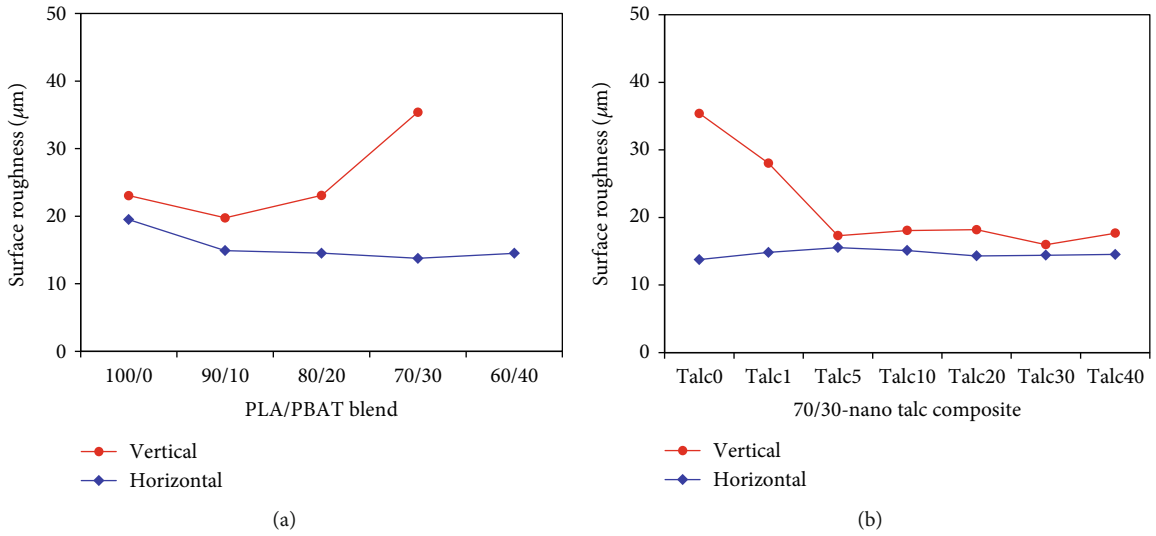

Figure 11: Surface roughness of vertical and horizontal dumbbell specimens: (a) PLA/PBAT blends; (b) 70/30-nano talc composites.

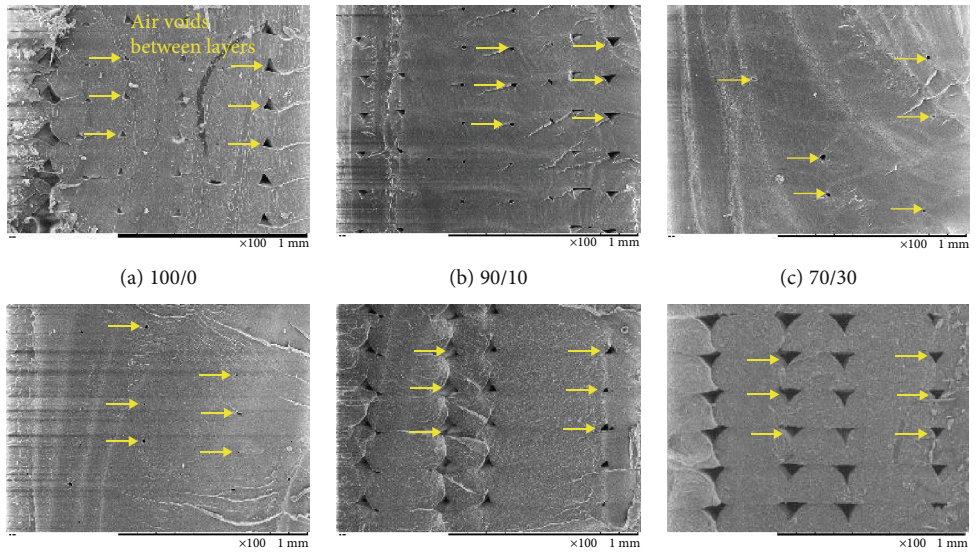

Figure 12: SEM images of cross-sectional surface of vertical dumbbell specimens (examples of air voids are located by arrows).

might be implied from the tensile strength of the vertical dumbbell specimens [2]. From the horizontal printing direction, tensile strength of these systems was comparable to products from commercial available filaments. Additionally, the elongation of the PLA/PBAT blends and the composites was higher than the products from the commercial as tabulated in Table 5. From the results, 3D printable filaments prepared in this study were comparable to use in FDM 3D printing technology.

4. Conclusion

It was suggested that the novel superior toughened 3D printable filaments of the PLA/PBAT-nano talc composites were successfully prepared, showing the excellent dimensional stability and printability, and presented high tensile properties of printing products as compared with neat PLA and the commercial 3D printing filaments. The nano talc plays the key role in the production of 3D printing products. The complex viscosity, crystallization temperature, and degree of crystallization of the composites increased while the coefficient of volume expansion decreased with the addition of the nano talc in the 70/30-nano talc composites, resulting in the improvement of dimension stability, surface roughness, and elongation at break of the composites. It was possible to print the PLA/PBAT-nano talc filaments even at the angle up to 75° during the overhang test without a supporter. However, 3D pintable filaments with nano talc contents

Table 5: Tensile properties of the blends and the composite 3D specimens and the commercial data* [52–58].

No.	Materials	Horizontal		Vertical	
		Tensile strength (MPa)	Elongation at break (%)	Tensile strength (MPa)	Elongation at break (%)
1	100/0	57.9 ± 5.53	3.6 ± 0.15	34.4 ± 3.20	2.4 ± 0.20
2	90/10	55.8 ± 4.00	4.1 ± 0.80	30.1 ± 2.11	1.9 ± 0.10
3	80/20	54.2 ± 4.80	7.0 ± 2.10	25.6 ± 2.30	1.8 ± 0.10
4	70/30	46.9 ± 2.00	225.8 ± 25.90	19.4 ± 1.90	1.6 ± 0.20
5	60/40	39.7 ± 2.30	348.4 ± 41.80	11.3 ± 1.80	1.8 ± 0.60
6	70/30-talc1	45.3 ± 3.10	410.0 ± 44.60	20.6 ± 2.10	2.2 ± 0.30
7	70/30-talc5	46.3 ± 2.90	348.5 ± 39.10	19.5 ± 1.10	2.0 ± 0.20
8	70/30-talc10	41.7 ± 3.50	177.4 ± 31.00	16.2 ± 0.50	1.7 ± 0.20
9	70/30-talc20	40.2 ± 2.00	104.7 ± 19.50	14.2 ± 2.00	1.5 ± 0.20
10	70/30-talc30	39.1 ± 3.10	44.1 ± 15.40	13.0 ± 1.20	1.1 ± 0.00
11	70/30-talc40	38.6 ± 1.10	22.0 ± 13.80	12.0 ± 1.70	1.0 ± 0.11
12	PLA (Ultimaker)*	49.5	5.2	—	—
13	ABS (Ultimaker)*	39.0	4.8	—	—
14	PolyMax™ PLA (Polymaker)*	28.1	1.4	—	—
15	PolyLite™ PLA (Polymaker)*	46.6	1.9	—	—
16	PolyLite™ ABS (Polymaker)*	33.3	2.7	—	—
17	ECOMAX® PLA (3DXTECH)*	56.0	8.0	—	—
18	3DXMAX® ABS (3DXTECH)*	42.0	10.0	—	—
19	Innofil3D PLA (BASF)*	38.1	2.8	28.8	1.1
20	Innofil3D ABS (BASF)*	29.3	3.7	6.5	0.7

*Tensile properties of the commercial data, horizontal printed in x, y-axis and vertical printed in z-axis [52–58].

more than 10 wt% presented excellent dimension stability but exhibited a lack of tensile properties. In this study, the optimum formulation of PLA/PBAT-nano talc 3D printable filaments should be in the range of PBAT 10 wt% to 30 wt% and the content of nano talc 1 wt% to 10 wt%.

Data Availability

The data used to support the findings of this study are available from the corresponding author upon request.

Conflicts of Interest

The authors declare no conflict of interest.

Acknowledgments

This research was financially supported by JSPS Grant-in-Aid for Scientific Research on Innovative Areas Grant Number JP18H05483. The authors would like to give thanks for the support of the doctoral scholarship from Pathumwan Institute of Technology, Thailand, for Mr. Wattanachai Prasong.

Supplementary Materials

Figure S1: scanning profile of surface roughness measurement. Figure S2: schematic observation of interlayer and voids from cross-sectional vertical dumbbell specimen. Figure S3: SEM images of alignment layers in the PLA/PBAT blends. Figure S4: SEM images of alignment layers in the 70/30-nano talc composites. *(Supplementary Materials)*

References

[1] S. C. Ligon, R. Liska, J. Stampfl, M. Gurr, and R. Mülhaupt, "Polymers for 3D printing and customized additive manufacturing," *Chemical Reviews*, vol. 117, no. 15, pp. 10212–10290, 2017.

[2] Q. Ou-Yang, B. Guo, and J. Xu, "Preparation and characterization of poly(butylene succinate)/polylactide blends for fused deposition modeling 3D printing," *ACS Omega*, vol. 3, no. 10, pp. 14309–14317, 2018.

[3] S. H. Kochesfahani, *Improving PLA-based material for FDM 3D-printers using minerals (principles and method development)*, SPE ANTEC™ Indianapolis, 2016.

[4] I. Chiulan, A. Frone, C. Brandabur, and D. Panaitescu, "Recent advances in 3D printing of aliphatic polyesters," *Bioengineering*, vol. 5, no. 1, p. 2, 2018.

[5] W. Xu, A. Pranovich, P. Uppstu et al., "Novel biorenewable composite of wood polysaccharide and polylactic acid for three dimensional printing," *Carbohydrate Polymers*, vol. 187, pp. 51–58, 2018.

[6] M. Qahtani, F. Wu, M. Misra, S. Gregori, D. F. Mielewski, and A. K. Mohanty, "Experimental design of sustainable 3D-printed poly(lactic acid)/biobased poly(butylene succinate)

blends via fused deposition modeling," *ACS Sustainable Chemistry & Engineering*, vol. 7, no. 17, pp. 14460–14470, 2019.

[7] E. V. Diederichs, M. C. Picard, B. P. Chang, M. Misra, D. F. Mielewski, and A. K. Mohanty, "Strategy to improve printability of renewable resource-based engineering plastic tailored for FDM applications," *ACS Omega*, vol. 4, no. 23, pp. 20297–20307, 2019.

[8] N. Aliheidari, J. Christ, R. Tripuraneni, S. Nadimpalli, and A. Ameli, "Interlayer adhesion and fracture resistance of polymers printed through melt extrusion additive manufacturing process," *Materials and Design*, vol. 156, pp. 351–361, 2018.

[9] C. Bellehumeur, L. Li, Q. Sun, and P. Gu, "Modeling of Bond Formation Between Polymer Filaments in the Fused Deposition Modeling Process," *Journal of Manufacturing Processes*, vol. 6, no. 2, pp. 170–178, 2004.

[10] T. Andrew and U. Ertu, *3D Printing- Media Hype or Manufacturing Reality: Textiles Surface Fashion Product Architecture*, Textile Centre of Excellence, Huddersfield UK, 2014.

[11] M. Xia and J. Sanjayan, "Method of formulating geopolymer for 3D printing for construction applications," *Materials and Design*, vol. 110, pp. 382–390, 2016.

[12] B. Coppola, N. Cappetti, L. di Maio, P. Scarfato, and L. Incarnato, "3D printing of PLA/clay nanocomposites: influence of printing temperature on printed samples properties," *Materials*, vol. 11, no. 10, p. 1947, 2018.

[13] N. Mohan, P. Senthil, S. Vinodh, and N. Jayanth, "A review on composite materials and process parameters optimisation for the fused deposition modelling process," *Virtual and Physical Prototyping*, vol. 12, no. 1, pp. 47–59, 2017.

[14] G. Cicala, D. Giordano, C. Tosto, G. Filippone, A. Recca, and I. Blanco, "Polylactide (PLA) filaments a biobased solution for additive manufacturing: correlating rheology and thermomechanical properties with printing quality," *Materials*, vol. 11, no. 7, p. 1191, 2018.

[15] M. A. Cuiffo, J. Snyder, A. M. Elliott, N. Romero, S. Kannan, and G. P. Halada, "Impact of the fused deposition (FDM) printing process on polylactic acid (PLA) chemistry and structure," *Applied Sciences*, vol. 7, no. 6, p. 579, 2017.

[16] C. B. Sweeney, B. A. Lackey, M. J. Pospisil et al., "Welding of 3D-printed carbon nanotube–polymer composites by locally induced microwave heating," *Science Advances*, vol. 3, no. 6, e1700262, 2017.

[17] J. Wootthikanokkhan, T. Cheachun, N. Sombatsompop et al., "Crystallization and thermomechanical properties of PLA composites: effects of additive types and heat treatment," *Journal of Applied Polymer Science*, vol. 129, no. 1, pp. 215–223, 2013.

[18] C. Benwood, A. Anstey, J. Andrzejewski, M. Misra, and A. K. Mohanty, "Improving the impact strength and heat resistance of 3D printed models: structure, property, and processing correlationships during fused deposition modeling (FDM) of poly(lactic acid)," *ACS Omega*, vol. 3, no. 4, pp. 4400–4411, 2018.

[19] Y. Ding, W. Feng, B. Lu, P. Wang, G. Wang, and J. Ji, "PLA-PEG-PLA tri-block copolymers: effective compatibilizers for promotion of the interfacial structure and mechanical properties of PLA/PBAT blends," *Polymer*, vol. 146, pp. 179–187, 2018.

[20] H. Moustafa, N. el Kissi, A. I. Abou-Kandil, M. S. Abdel-Aziz, and A. Dufresne, "PLA/PBAT bionanocomposites with antimicrobial natural rosin for green packaging," *ACS Applied Materials & Interfaces*, vol. 9, no. 23, pp. 20132–20141, 2017.

[21] W. Liu, P. Chen, X. Wang, F. Wang, and Y. Wu, "Effects of poly(butyleneadipate-co-terephthalate) as a macromolecular nucleating agent on the crystallization and foaming behavior of biodegradable poly(lactic acid)," *Cellular Polymers*, vol. 36, no. 2, pp. 75–96, 2017.

[22] D. Nakayama, F. Wu, A. K. Mohanty, S. Hirai, and M. Misra, "Biodegradable composites developed from PBAT/PLA binary blends and silk powder: compatibilization and performance evaluation," *ACS Omega*, vol. 3, no. 10, pp. 12412–12421, 2018.

[23] E. Quero, A. J. Müller, F. Signori, M. B. Coltelli, and S. Bronco, "Isothermal cold-crystallization of PLA/PBAT blends with and without the addition of acetyl tributyl citrate," *Macromolecular Chemistry and Physics*, vol. 213, no. 1, pp. 36–48, 2012.

[24] M. Hernández-López, Z. N. Correa-Pacheco, S. Bautista-Baños et al., "Bio-based composite fibers from pine essential oil and PLA/PBAT polymer blend. Morphological, physicochemical, thermal and mechanical characterization," *Macromolecular Chemistry and Physics*, vol. 234, pp. 345–353, 2019.

[25] S. Singamneni, D. Smith, M. J. LeGuen, and D. Truong, "Extrusion 3D printing of polybutyrate-adipate-terephthalate-polymer composites in the pellet form," *Polymers*, vol. 10, no. 8, p. 922, 2018.

[26] D. Battegazzore, S. Bocchini, and A. Frache, "Crystallization kinetics of poly(lactic acid)-talc composites," *Express Polymer Letters*, vol. 5, no. 10, pp. 849–858, 2011.

[27] Y. Zhou, X. Xia, X. Liu et al., "Preparation and rheological and mechanical properties of poly(butylene succinate)/talc composites for material extrusion additive manufacturing," *Macromolecular Materials and Engineering*, vol. 304, no. 7, 2019.

[28] M. Murariu and P. Dubois, "PLA composites: from production to properties," *Advanced Drug Delivery Reviews*, vol. 107, pp. 17–46, 2016.

[29] F. Yu, T. Liu, X. Zhao, X. Yu, A. Lu, and J. Wang, "Effects of talc on the mechanical and thermal properties of polylactide," *Journal of Applied Polymer Science*, vol. 125, no. S2, pp. E99–E109, 2012.

[30] S. Saravana, G. Bheemaneni, and R. Kandaswamy, "Effect of polyethylene glycol on mechanical, thermal, and morphological properties of talc reinforced polylactic acid composites," *Materials Today: Proceedings*, vol. 5, no. 1, pp. 1591–1598, 2018.

[31] B. Redwood, F. Schöffer, and B. Garret, *The 3D Printing Handbook: Technologies, Design and Applications*, 3D HUBS, 2017.

[32] G. Ćwikła, C. Grabowik, K. Kalinowski, I. Paprocka, and P. Ociepka, "The influence of printing parameters on selected mechanical properties of FDM/FFF 3D-printed part," *Materials Science and Engineering*, vol. 227, 2017.

[33] A. Teamsinsungvon, Y. Ruksakulpiwat, and K. Jarukumjorn, "Poly(lactic acid)/Poly(butylene adipate-*co*-terephthalate) Blend and its Composite: Effect of Maleic Anhydride Grafted Poly(lactic acid) as a Compatibilizer," *Advanced Materials Research*, vol. 410, pp. 51–54, 2011.

[34] Y. Deng, C. Yu, P. Wongwiwattana, and N. L. Thomas, "Optimising ductility of poly(lactic acid)/poly(butylene adipate-co-terephthalate) blends through co-continuous phase morphology," *Journal of Polymers and the Environment*, vol. 26, no. 9, pp. 3802–3816, 2018.

[35] A. L. P. D. L. Freitas, L. R. Tonini Filho, P. S. Calvão, and A. M. C. de Souza, "Effect of montmorillonite and chain extender on rheological, morphological and biodegradation behavior of PLA/PBAT blends," *Polymer Testing*, vol. 62, pp. 189–195, 2017.

[36] L. C. Arruda, M. Magaton, R. E. S. Bretas, and M. M. Ueki, "Influence of chain extender on mechanical, thermal and morphological properties of blown films of PLA/PBAT blends," *Polymer Testing*, vol. 43, pp. 27–37, 2015.

[37] S.-Y. Gu, K. Zhang, J. Ren, and H. Zhan, "Melt rheology of polylactide/poly(butylene adipate- *co* -terephthalate) blends," *Carbohydrate Polymers*, vol. 74, no. 1, pp. 79–85, 2008.

[38] L. Jiang, M. P. Wolcott, and J. Zhang, "Study of biodegradable polylactide/poly(butylene adipate-co-terephthalate) blends," *Biomacromolecules*, vol. 7, no. 1, pp. 199–207, 2006.

[39] R. Al-Itry, K. Lamnawar, and A. Maazouz, "Biopolymer blends based on poly (lactic acid): shear and elongation rheology/-structure/blowing process relationships," *Polymers*, vol. 7, no. 5, pp. 939–962, 2015.

[40] E. J. Padilha Júnior, R. . P. Soares, and N. S. M. Cardozo, "Analysis of equations of state for polymers," *Polímeros*, vol. 25, no. 3, pp. 277–288, 2015.

[41] D. Tripathi and T. K. Dey, "Thermal conductivity, coefficient of linear thermal expansion and mechanical properties of LDPE/Ni composites," *Indian Journal of Physics*, vol. 87, no. 5, pp. 435–445, 2013.

[42] M. Katayama, J. Nakakuki, J.-H. Pee, and Y. Kobayashi, "Effect of particle size of tabular talc powders on crystal orientation and sintering of cordierite ceramics," *Journal of the Ceramic Society of Japan*, vol. 121, no. 1419, pp. 934–939, 2013.

[43] G. Chen, D. Zhiwei, X. Lei, S. Guo, and G. Li, "Modification of a theoretical model for the prediction of the thermal expansion behavior of particulate composites: application to poly(vinyl chloride)/talc composites," *Journal of Macromolecular Science, Part B*, vol. 52, no. 9, pp. 1309–1321, 2013.

[44] A. Shakoor and N. L. Thomas, "Talc as a nucleating agent and reinforcing filler in poly(lactic acid) composites," *Polymer Engineering and Science*, vol. 54, no. 1, pp. 64–70, 2014.

[45] C. Xu, X. Zhang, X. Jin, S. Nie, and R. Yang, "Study on mechanical and thermal properties of poly(lactic acid)/poly(-butylene adipate-co-terephthalate)/office wastepaper fiber biodegradable composites," *Journal of Polymers and the Environment*, vol. 27, no. 6, pp. 1273–1284, 2019.

[46] H. Xiao, W. Lu, and J.-T. Yeh, "Crystallization behavior of fully biodegradable poly(lactic acid)/ poly(butylene adipate-co-terephthalate) blends," *Journal of Applied Polymer Science*, vol. 112, no. 6, pp. 3754–3763, 2009.

[47] S. Jain, M. Misra, A. K. Mohanty, and A. K. Ghosh, "Thermal, mechanical and rheological behavior of poly(lactic acid)/talc composites," *Journal of Polymers and the Environment*, vol. 20, no. 4, pp. 1027–1037, 2012.

[48] Y.-H. Cai, "Crystallization and melting behavior of biodegradable poly(l-lactic acid)/talc composites," *E-Journal of Chemistry*, vol. 9, no. 3, pp. 1569–1574, 2012.

[49] I. R. Mustapa and R. A. Shanks, "Dynamic mechanical properties and melting behaviour of poly(lactic acid)-hemp-nanosilica hybrid composites," in *15th European of conference on composite materials (ECCM15)*, pp. 1–8, Venice, Italy, 2012.

[50] M. S. Alsoufi and A. E. Elsayed, "Surface roughness quality and dimensional accuracy: a comprehensive analysis of 100% infill printed parts fabricated by a personal/desktop cost-effective FDM 3D printer," *Materials Sciences and Applications*, vol. 9, no. 1, pp. 11–40, 2018.

[51] F. R. Ramli, M. S. M. Faudzie, M. A. Nazan et al., "Dimensional accuracy and surface roughness of part features manufactured by open source 3D printer," *APR Journal of Engineering and Applied Sciences*, vol. 13, no. 3, pp. 1139–1144, 2018.

[52] Ultimaker, *Technical and safety data sheets, Ultimaker PLA*, 2018, https://ultimaker.com/en/resources/50461-technical-and-safety-data-sheets.

[53] Polymaker, *Technical data sheet, PolyMax™ PLA*, 2018, https://polymaker.com/product/polymax-PLA.

[54] Polymaker, *Technical data sheet, PolyLite™ PLA*, 2018, https://polymaker.com/product/polylite-PLA.

[55] Polymaker, Technical data sheet, PolyLite™ ABS, *Technical data sheet*, 2018, https://polymaker.com/product/polylite-abs.

[56] 3DXTECH Advanced materials, Tech Data Sheets & Safety Data Sheets, 2018, https://www.3dxtech.com/tech-data-sheets-safety-data-sheets.

[57] BASF - Innofil3D, Technical data sheet PLA by Innofil3D BV, 2017, https://www.ultrafusefff.com/wp-content/uploads/2016/05/TDS-Innofil3D-PLA-160608.pdf.

[58] BASF - Innofil3D, Technical data sheet ABS by Innofil3D BV, 2016, https://www.ultrafusefff.com/wp-content/uploads/2016/05/TDS-Innofil3D-ABS-160609.pdf.

Hindawi
Journal of Nanomaterials
Volume 2020, Article ID 6742728, 9 pages
https://doi.org/10.1155/2020/6742728

Research Article

Enhancement of Photoelectrochemical Performance of Ag@ZnO Nanowires: Experiment and Mechanism

Yu Cai,[1] Chengbao Yao ,[1] and Jie Yuan[2]

[1]*Key Laboratory of Photonic and Electric Bandgap Materials, Ministry of Education, School of Physics and Electronic Engineering, Harbin Normal University, Harbin, 150025 Heilongjiang, China*
[2]*Harbin Medical University, Daqing Campus, Daqing, 163319 Heilongjiang, China*

Correspondence should be addressed to Chengbao Yao; yaochengbao5@163.com

Received 5 December 2019; Revised 22 February 2020; Accepted 3 March 2020; Published 20 March 2020

Guest Editor: Edson C. da Silva Filho

This paper focuses on the enhancement of photoelectrochemical (PEC) performance of uniform silver nanoparticles-decorated ZnO (Ag@ZnO) nanowires, which have been synthesized by two-step chemical vapor deposition to prepare ZnO nanowires then magnetron sputtering method to deposit Ag nanoparticles. Moreover, we analyzed the mechanisms of the PEC behavior of the Ag@ZnO nanowires. The PEC characteristics show that the current density of Ag@ZnO nanowires increased comparing to that of unmodified ZnO nanowires. The optimized content of the Ag-decorated ZnO photoelectrode is up to the maximum photocurrent density of 24.8 μAcm^{-2} at 1 V vs. Ag/AgCl, which was almost four times than that of the unmodified ZnO photoelectrode. Based on the surface plasmon resonance (SPR), effect of Ag nanoparticles was enhanced PEC performance of the Ag@ZnO nanowires. Because SPR effect of Ag nanoparticles extended the light absorption and enhanced the separation efficiency of the photogenerated electron-hole pairs. The remarkable PEC properties offer metals-semiconductor compound nanostructures materials as a promising electron source for high current density applications.

1. Introduction

As always, zinc oxide (ZnO) materials have been studied continuously by many researchers because of its advantages of excellent characteristics and excellent features and wide range of applications [1–15]. However, to improve its electrical and optical properties, ZnO is generally doped or decorated with group various elements. Doped ZnO materials are promising candidates as conductors with high transparency in the visible light range and high conductivity [16, 17]. The conductivity, ferromagnetic, and transparency properties of doped ZnO materials have been increased in terms of present reports [18–22]. Decorated ZnO materials are promising candidates as conductors with the absorption of visible light being enhanced and the combination of photogenerated electron-holes being suppressed [23, 24]. Recently, varieties of metal-doped or decorated semiconductor compounds nanostructures morphologies [5, 25–31], such as nanowires, nanotubes, nanorods, nanoflowers, nanorings, nanobelts, nanosheets, nanowalls, nanograsses, and heterostructures, have been successfully synthesized using multiple methods, including chemical vapor deposition (CVD) [32, 33], screen printing technologies [34, 35], hydrothermal method [36, 37], hydrothermal and chemical method [38], the thermal evaporation process [39], thermal evaporation method [40], and a template-free single-step hydrothermal method [41]. However, CVD and magnetron sputtering (MS) methods are very common methods for growth of nanomaterial with different morphologies. In addition, among the various metal elements, compared to semiconductor nanoparticles, noble metal nanoparticles have considerable photostability [42–45]. The noble metal-decorated semiconductor nanomaterials increased the photon absorption rate of the photoanode and improved the photoactivity because the surface plasmon resonance (SPR) effect of metal nanoparticles induced electric field application near the oxide semiconductor surface [46]. Due to localized SPR effect, Ag nanoparticles possess strong absorptions in the visible spectrum and could improve the apparent photoactivity of the semiconductor in the visible region. There

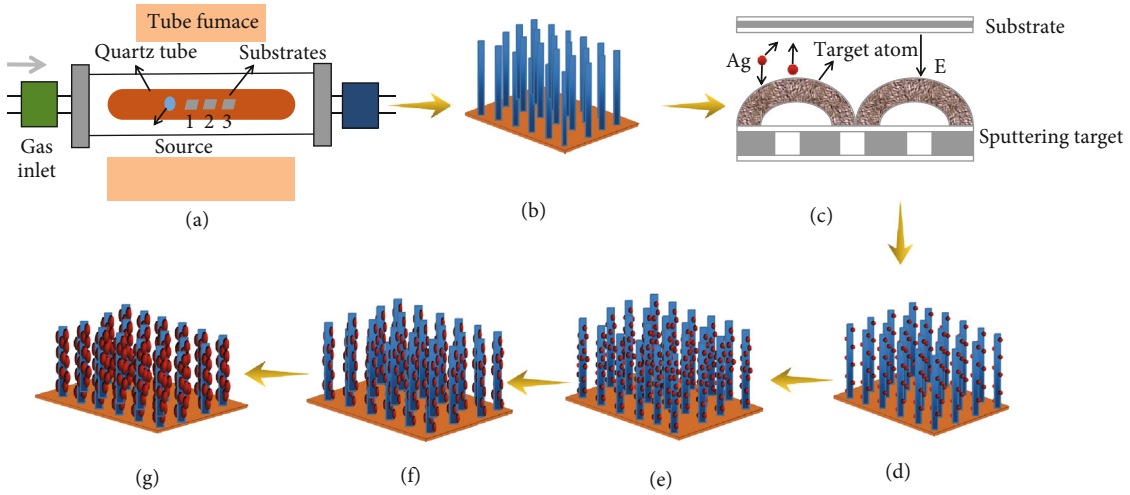

Figure 1: Growth process of Ag@ZnO NWs at the sputtering time.

are many articles reporting physical properties of silver nanoparticle-decorated ZnO with different nanostructure [47–53]. Ag nanoparticles are selected to decorate semiconductors which were widely applied in PEC devices.

In a previous report, uniform silver nanoparticles-decorated ZnO (Ag@ZnO) nanowires composite which were successfully synthesized by two-step CVD and MS method are reported [54, 55]. We studied the structure and optical properties of Ag@ZnO nanowires by magnetron sputtering method at sputtering time of 80, 100, and 120 s. However, there are no detail reports on the study of deposition parameters, which will impact on the film properties. The analysis about the PEC behavior of the Ag@ZnO nanowires is seldom reported. In the present paper, using transmission electron microscopy (TEM) and X-ray diffraction (XRD) techniques, the observed morphology and structure of Ag@ZnO nanowires were analyzed. The PEC performance of the samples was investigated. Ag@ZnO nanowires exhibit excellent PEC performance compared to unmodified ZnO nanowires, which are likely to be the potential applications in photoelectric devices.

2. Experimental Section

2.1. Grown of Samples. The Ag@ZnO nanowires were synthesized on quartz substrates by two-step CVD and MS method. The ZnO nanowires were grown by the CVD, and then Ag nanoparticles were deposited on ZnO nanowires using the MS system. As shown in Figure 1, ZnO NWs decorated with Ag nanoparticles were manufactured in the two steps of CVD and MS. The precursor is the powder of ZnO (1 g) on 1D nanostructure for nanowires. It was placed into an alumina boat and loaded into the tubular furnace. The Au-coated quartz substrates were placed downstream from the powders. The furnace was heated to a preset temperature (1250°C). Ar was used as carrier gas during growth at the constant flow rate and pressure: 100 sccm, 50 Pa for ZnO nanowires. Afterwards, the furnace was naturally cooled down to room temperature. Radio frequency target (RFT) is an Ag disc of

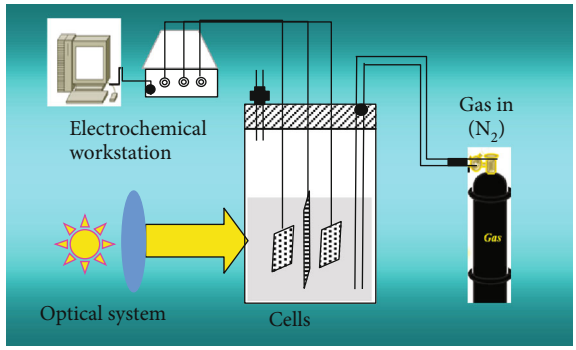

Figure 2: Schematic of the measurement of PEC for the unmodified ZnO and Ag-ZnO nanowires.

60 mm in diameter with a purity of 99.99%. The base pressure in the deposition chamber and radio frequency power were 6.0×10^{-4} Pa and 3 W, respectively. The growth of sample proceeded in the growth ambient with the Ar of 20 sccm at a constant working pressure of 1.0 Pa, and the sputtering times are 80,100, and 120 s, respectively.

2.2. Characteristic of Samlpes. The morphologies and components of Ag@ZnO and unmodified ZnO nanowires were observed by using field emission scanning electron microscopy (FE-SEM), energy dispersive X-ray (EDX), and TEM. The crystallinity was analyzed by using XRD equipped with monochromated Cu Ka irradiation. PEC properties of sample photoanodes were carried out in a three-electrode cell at room temperature. Figure 2 illustrates the schematic diagram of experimental setup. Briefly, 0.05 mol/L Na_2SO_4 solutions were used as electrolytes, through which nitrogen was bubbled. The illumination source was a 200-W Xe arc lamp.

3. Results and Discussion

3.1. The Morphologies and Structure for Ag@ZnO Nanowires. Figures 3(a)–3(d) show the FE-SEM images of the unmodified ZnO and Ag@ZnO nanowires with different sputtering

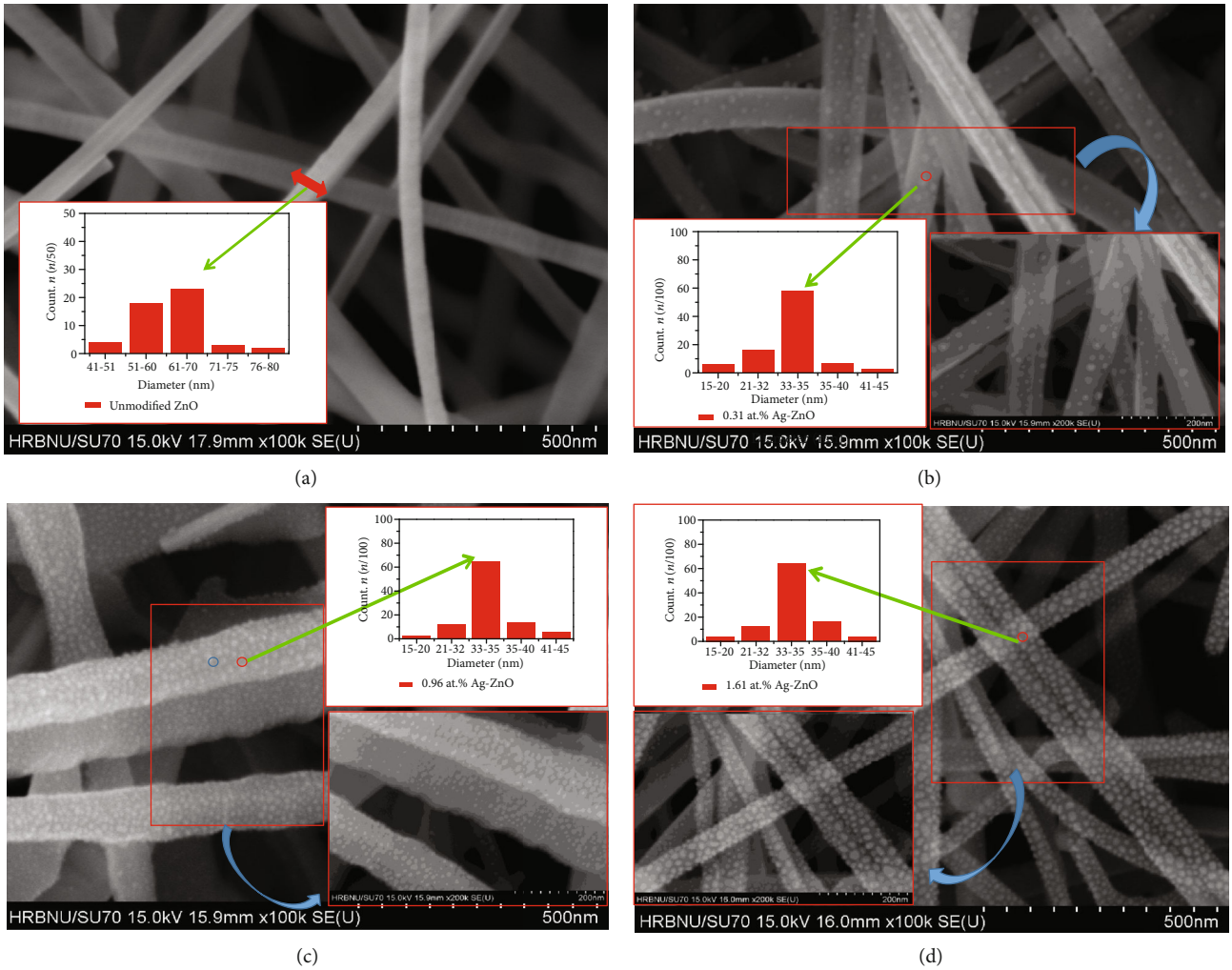

FIGURE 3: Low-magnification image FE-SEM image of (a) unmodified ZnO and (b–d) Ag@ZnO nanowires. The inset shows the distribution of the average diameter and particle size for unmodified ZnO and Ag@ZnO nanowires.

times of Ag (80,100, and 120 s), respectively. Because the average diameter and length of unmodified ZnO nanowires were approximately 65 nm and 2 μm (see the inset of Figure 3(a)), the ZnO nanowires have excellent aspect ratios. In the local magnification, Ag particles can be clearly seen, which is around 33~35 nm of most size and have a little change (see the insetof Figures 3(b)–3(d)). However, with the increase of time, Ag particle density increases and the coverage area of Ag@ZnO nanowires increases; among them, Ag particles in Figure 3(d) are the most uniform. The Ag@ZnO nanowires unfold rougher surfaces which are attributed to the adsorption of Ag nanoparticles on the surface of the ZnO nanowires.

To confirm the attachment between nanoparticles and ZnO nanowires on the surface, TEM was used, and the observed results were shown in Figures 4(a)–4(c). The figures are the TEM images of a single silver composite ZnO nanowire after ultrasonic dispersion. As can be seen from Figure 4(a), only a small number of silver nanoparticles were attached to the surface of ZnO nanowires when the sputtering time was 80 s. With the continuous increase of sputtering time of silver particles, the particle distribution density and particle size on the surface of ZnO nanowires gradually increased. When the sputtering time was 120 s, the silver particles on the surface appeared clustering. As shown in the magnification of surface particles of Ag/ZnO under high-power electron microscope, Figure 4(a) shows that the silver sputtering time was the shortest, and the crystal array of ZnO could be seen most clearly. The SAED pattern indicates that the crystal lattice of ZnO is clear and the lattice spacing is 0.28 nm, which corresponds to the diffraction crystal surface (100) of ZnO. As the sputtering time was prolonged, the number of silver particles on the surface of the nanowires increased, covering the surface of ZnO, and the crystal texture was not as clear as that in Figure 4(b). But the ZnO lattice arrangement can also be seen clearly in Figure 4(b). Moreover, in Figure 3(c), in addition to the (100) crystal plane, there is also a ZnO (110) crystal plane with lattice spacing of 0.16 nm and a silver diffraction ring.

The XRD was used to study the structure of ZnO nanowires which were modified or not with Ag. As shown in Figures 5(a)–5(d), these results indicated that the Ag@ZnO

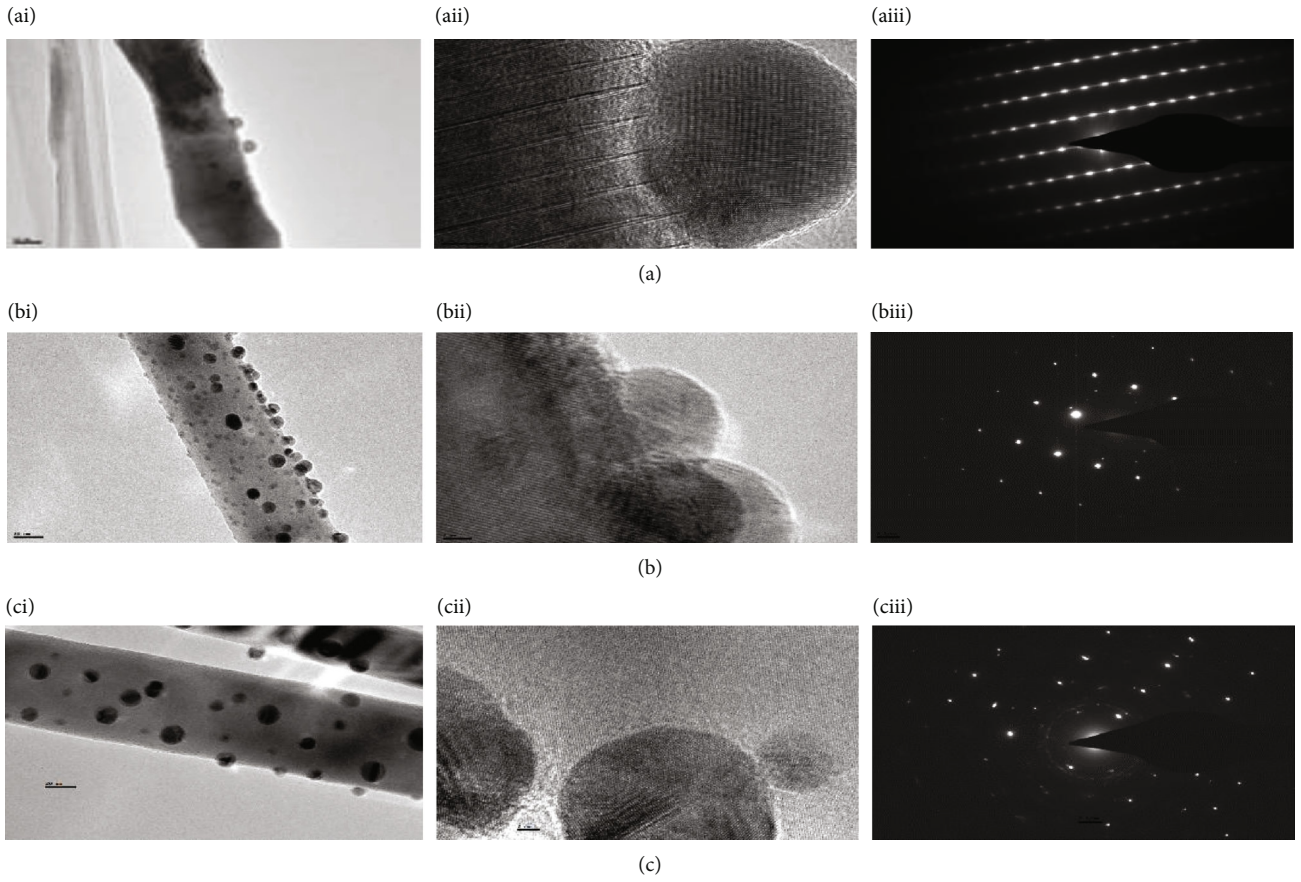

Figure 4: The TEM (ai–ci), HRTEM (aii–cii), and selected-area electron diffraction (SAED) patterns (aiii–ciii) of Ag@ZnO nanowires with sputtering times of 80, 100, and 120 s.

nanowires had high crystal crystallinity and were highly oriented to the [0002] crystal c-axis direction. The XRD results are in agreement with the TEM analysis. The observed diffraction peaks are indexed to a hexagonal wurtzite phase of ZnO, with lattice constants of $a = 0.324$ nm and $c = 0.548$ nm (JCPDS card no. 36-1451). The XRD pattern depicts a set of well-defined diffraction peaks which indicated the crystalline nature of the as-synthesized nanowires, in contrast with the other diffraction peaks, because Ag and Zn exist in the synthesized Ag@ZnO nanowires. The XRD patterns illustrated that the peaks at two theta (2θ) values of 38.24° can be attributed to the prominent (111) diffraction patterns of nanocrystalline Ag particles. When the Ag content was further increased, the diffraction peak intensity of ZnO slightly decreased, while the diffraction peak intensity of Ag increased, which was due to the increase of covered surface by the Ag particles and consistent with SEM and EDX analysis. Moreover, the diffraction peaks in the XRD figure are clear and sharp, indicating that the crystallinity is good, the crystal defects are few, and no impurity peaks proves that the purity is very high.

The typical EDX results of the unmodified ZnO and Ag@ZnO nanowires were plotted in Figures 6(a)–6(d). From EDX spectra, there are clear peaks of the element (O and Zn for unmodified ZnO; O, Zn, and Ag for Ag@ZnO). The EDX data confirmed that the unmodified ZnO nanowires contained 63.61 at. % zinc and 39.39 at. % oxygen. And the Ag@ZnO nanowires contained 0.31 at. %, 0.96 at. %, and 1.61 at. % silver. The atomic percent of Ag was gradually increased with the sputtering time being longer. It is worth mentioning that with the increase of silver sputtering time, the content of zinc atoms in the sample material gradually decreases while the content of oxygen atoms gradually increases. In theory, in ZnO material, the atomic ratio of Zn and O should be 1 : 1, but intrinsic donor-type defects of the ZnO exist, namely the oxygen vacancy and zinc clearance, causing more zinc and O atoms than the theoretical value. In this experiment, sputtering time increasing of silver particles made the ratio of zinc and O atoms that were gradually adjusted from greater than 2 : 1 to approximately 1 : 1, so that it was based on silver nanoparticles composite, improved the intrinsic defects of zinc oxide.

3.2. Photoelectrochemical Performance. The PEC performance of unmodified ZnO and Ag@ZnO nanowires photoanodes has been studied by evaluating the current density-voltage (J–V) characteristics under light illumination. The J–V characteristics of the sample photoanodes are shown in Figure 7. As can be seen from Figure 6(a), for the 1.0 V vs Ag/AgCI, the photocurrent density of A@ZnO nanowires reached the highest value of 24.8 μAcm^{-2}, which is almost six times higher than that of the unmodified ZnO photoelectrode

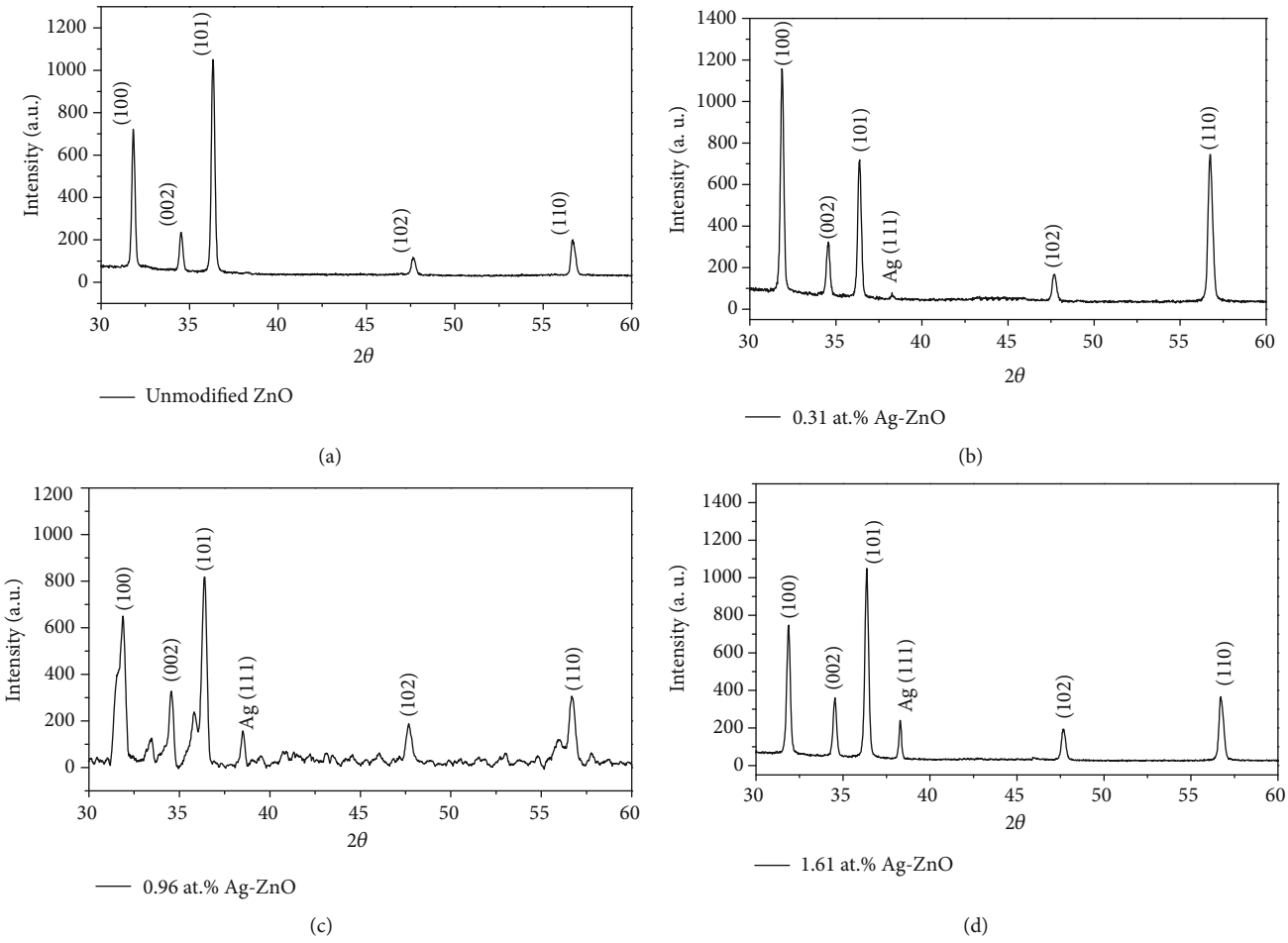

Figure 5: XRD patterns of (a) unmodified ZnO and (b–d) Ag@ZnO nanowires.

photocurrent density of 4.8 μAcm^{-2}. Dark scan linear sweep voltammagrams from -0.5 to +1.5 V showed a small current in the range of 0 to 40 μA/cm^2. When the Ag nanoparticles were modified, the SPR effect of Ag particles enhanced PEC properties. In a previous report, the charge transport within doped or decorated ZnO nanostructure is more efficient compared to ZnO nanostructured electrodes [56–59]. Figure 7(b) illustrates the instantaneous current density curves, namely *I-t* curve, visible from the figure, good light stability of the electrode to light and open to turn off the lights of the current density line, show no light-induced charge effect.

Figure 7(a) shows the photocurrent response of Ag/ZnO-coated nanowires with different silver contents. As can be seen from the Figure 7, with the increase of silver content, the photocurrent gradually increased. Among them, the optical response of 0.31 at. % Ag/ZnO is poor, the photocurrent density is very weak, and there is a certain response delay. When the silver content is 0.96 at. %, the delayed response disappears. When the silver content is 1.61 at. %, the photocurrent density increased significantly, which was about 1 mA/cm^2. It is proved that the increase of particle density and size on the surface of nanowires leads to better photosensitivity. As Ag particles are combined with ZnO nanowires, there is electron transfer when they contact with each other. At this time, the more Ag content there is, the more electrons it will carry. Under the action of external electric field, electrons will transfer to the opposite electrode, thus enhancing the photocurrent density.

The Ag@ZnO nanowires (for 0.96 at. % and 1.61 at. %) were selected for LSV test, and the test results are shown in Figure 7(b). At the same voltage, the current is stronger when there is more silver particles or light. The enhancement of photocurrent for Ag@ZnO nanowires was attributed to the following three factors: firstly, the local field is enhanced by SPR effect of Ag nanoparticles; secondly, the high separation efficiency of photogenic electron-hole pair; and thirdly, due to the interaction between ZnO and Ag, and reduce the charge resistance and charge compound rate. Figure 7(c) shows EIS test diagrams of Ag@ZnO nanowires with and without light. The arc radius of high silver content nanowires is smaller than that of silver content nanowires, and the arc radius with light is smaller than that without light. Since the arc radius in the figure reflects the resistance of the interface layer occurring on the electrode surface, the presence of Ag particles accelerates the electron-hole pair separation of ZnO nanowires, and the interface charge transfer is faster. The interaction between Ag and ZnO can effectively improve the separation and transfer efficiency of electron-hole pairs in ZnO and effectively inhibits the electron-hole pair

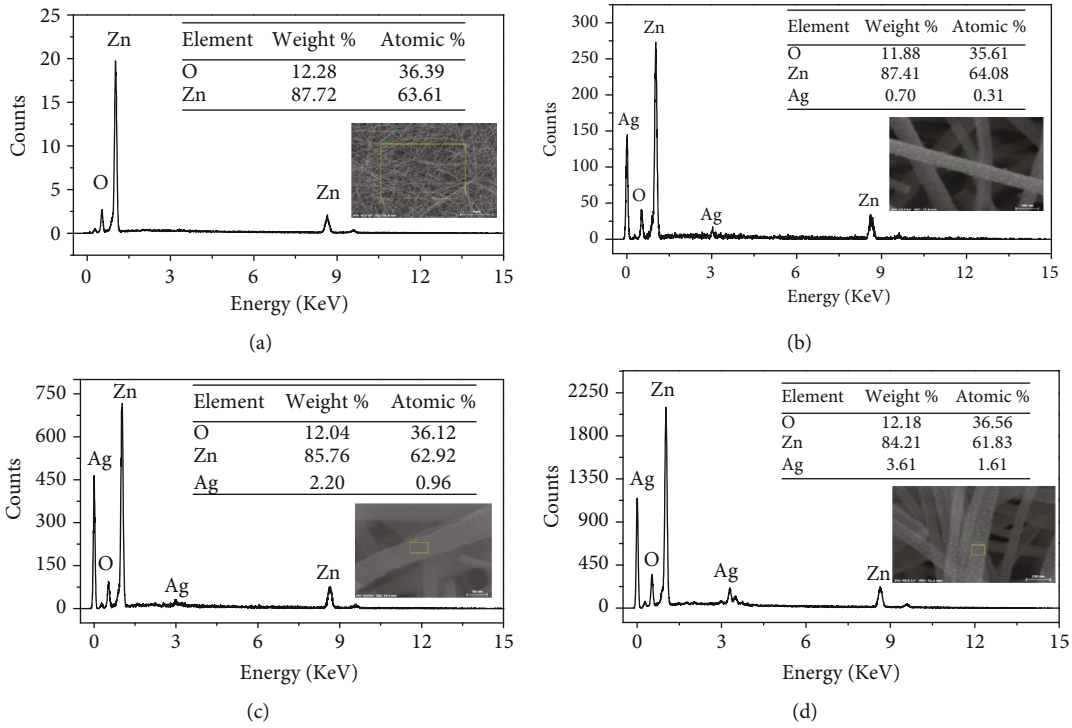

Figure 6: EDX spectra of (a) unmodified ZnO and (b–d) Ag@ZnO nanowires.

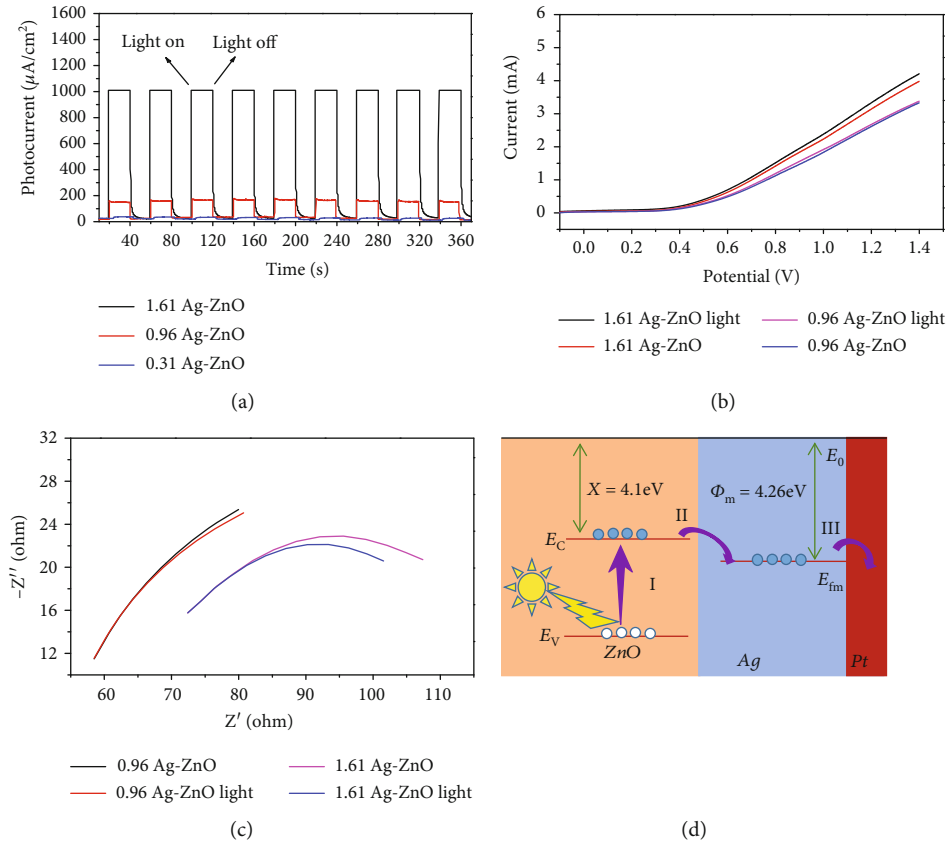

Figure 7: (a) Transient photoresponse, (b) linear sweep voltammograms, (c) EIS Nyquist plots, and (d) PEC mechanism diagram of Ag@ZnO nanowires electrodes.

recombination simultaneously. The results show that this method can effectively inhibit the electron-hole pair recombination and improve the photocatalytic activity of Ag@ZnO nanowires. We believe that Ag@ZnO nanowires can be used as effective materials to enhance photocurrent.

Based on the above discussions, the electron-transfer mechanism of the Ag@ZnO nanowires photoanode in PEC is just showed in Figure 7(d). Under the illumination, the electrons are excited to the CB of ZnO, and the same number of holes are created in the in the VB. The energy level of the bottom of the CB of ZnO is higher than the newly formed Fermi energy of the Ag@ZnO nanowires, so the photoexcited electrons would be transferred from ZnO to Ag, driven by the energy difference to enhance the separation efficiency of the photogenerated electron-hole pairs and reduces carrier recombination. Meanwhile, due to SPR excitation, Ag nanoparticles absorb the resonant photons to generate hot electrons, and hot electrons were transferred to the CB of ZnO.

4. Conclusions

In summary, the morphologies, structure, and PEC properties of successfully synthesized uniform Ag@ZnO nanowires by two-step CVD and MS methods were investigated. Our results indicate that the ZnO nanowires are highly crystalline with a lattice fringe of 0.28 nm, which corresponds to the (0002) planes in the ZnO crystal lattice. The average diameter of the Ag nanoparticles in the ZnO nanowires is estimated as ~34.86 nm. With the Ag nanoparticles decoration, visible emission peaks increased. Significantly, Ag@ZnO nanowires exhibit excellent PEC performance compared to unmodified ZnO nanowires. The PEC studies indicate that all electrodes are resistive in nature. The optimized content of the Ag@ZnO nanowires photoelectrode achieved the maximum photocurrent density of 24.8 μAcm^{-2} at 1 V vs. Ag/AgCl in 0.5 M Na_2SO_4, which was almost four times than that of the ZnO nanowires photoelectrode under the same conditions. The enhancement of the Ag@ZnO nanowires PEC performance was attributed to the SPR effect of Ag nanoparticles, which extended the light absorption and enhanced the separation efficiency of the photogenerated electron-hole pairs. Our results indicate that Ag@ZnO nanostructures show great potential as flat panel displays, high brightness electron sources, and photoanodes in PEC devices.

Data Availability

The data used to support the findings of this study are available from the corresponding author upon request.

Conflicts of Interest

The authors declare that they have no conflicts of interest.

Acknowledgments

This work was supported by the National Natural Science Foundation of China (11504072) and the University Nursing Program for Young Scholars with Creative Talents in Heilongjiang Province (No. UNPYSCT-2016179).

References

[1] C. Klingshirn, "ZnO: material, physics and applications," *ChemPhysChem*, vol. 8, no. 6, pp. 782–803, 2007.

[2] M. Law, L. E. Greene, J. C. Johnson, R. Saykally, and P. Yang, "Nanowire dye-sensitized solar cells," *Nature Materials*, vol. 4, no. 6, pp. 455–459, 2005.

[3] D. Panda and T. Y. Tseng, "One-dimensional ZnO nanostructures: fabrication, optoelectronic properties, and device applications," *Journal of Materials Science*, vol. 48, no. 20, pp. 6849–6877, 2013.

[4] D. T. Nguyen, E. C. Shin, D. C. Cho, K. W. Chae, and J. S. Lee, "Photoelectrochemical performance of ZnO thin film anodes prepared by solution method," *International Journal of Hydrogen Energy*, vol. 39, no. 35, pp. 20764–20770, 2014.

[5] A. B. Djurišić and Y. H. Leung, "Optical properties of ZnO nanostructures," *Small*, vol. 2, no. 8-9, pp. 944–961, 2006.

[6] C. L. Hsu and S. J. Chang, "Doped ZnO 1D nanostructures: synthesis, properties, and photodetector application," *Small*, vol. 10, no. 22, pp. 4562–4585, 2014.

[7] A. B. Djurišić, A. M. C. Ng, and X. Y. Chen, "ZnO nanostructures for optoelectronics: material properties and device applications," *Progress in Quantum Electronics*, vol. 34, no. 4, pp. 191–259, 2010.

[8] J. Li, H. Fan, and X. Jia, "Multilayered ZnO nanosheets with 3D porous architectures: synthesis and gas sensing application," *The Journal of Physical Chemistry C*, vol. 114, no. 35, pp. 14684–14691, 2010.

[9] A. Baltakesmez, S. Tekmen, and S. Tüzemen, "ZnO homojunction white light-emitting diodes," *Journal of Applied Physics*, vol. 110, no. 5, 2011.

[10] M. H. Huang, S. Mao, H. Feick et al., "Room-temperature ultraviolet nanowire nanolasers," *Science*, vol. 292, no. 5523, pp. 1897–1899, 2001.

[11] C. Soci, A. Zhang, B. Xiang et al., "ZnO nanowire UV photodetectors with high internal gain," *Nano Letters*, vol. 7, no. 4, pp. 1003–1009, 2007.

[12] M. S. Arnold, P. Avouris, Z. W. Pan, and Z. L. Wang, "Field-effect transistors based on single semiconducting oxide nanobelts," *The Journal of Physical Chemistry B*, vol. 107, no. 3, pp. 659–663, 2003.

[13] X. D. Bai, P. X. Gao, Z. L. Wang, and E. G. Wang, "Dual-mode mechanical resonance of individual ZnO nanobelts," *Applied Physics Letters*, vol. 82, no. 26, pp. 4806–4808, 2003.

[14] S. Suwanboon, P. Amornpitoksuk, and A. Sukolrat, "Dependence of optical properties on doping metal, crystallite size and defect concentration of M-doped ZnO nanopowders (M = Al, Mg, Ti)," *Ceramics International*, vol. 37, no. 4, pp. 1359–1365, 2011.

[15] A. Wei, X. W. Sun, J. X. Wang et al., "Enzymatic glucose biosensor based on ZnO nanorod array grown by hydrothermal decomposition," *Applied Physics Letters*, vol. 89, no. 12, p. 123902, 2006.

[16] P.-Y. Prodhomme, A. Beya-Wakata, and G. Bester, "Nonlinear piezoelectricity in wurtzite semiconductors," *Physical Review B*, vol. 88, no. 12, p. 121304, 2013.

[17] S. J. Pearton, D. P. Norton, M. P. Ivill et al., "ZnO doped with transition metal ions," *IEEE Transactions on Electron Devices*, vol. 54, no. 5, pp. 1040–1048, 2007.

[18] G. D. Yuan, W. J. Zhang, J. S. Jie et al., "Tunable n-type conductivity and transport properties of Ga-doped ZnO nanowire arrays," *Advanced Materials*, vol. 20, no. 1, pp. 168–173, 2010.

[19] M. Y. Tan, C. B. Yao, X. Y. Yan et al., "Structural and nonlinear optical behavior of Ag-doped ZnO films," *Optical Materials*, vol. 51, pp. 133–138, 2016.

[20] C. B. Yao, K. X. Zhang, X. Wen, J. Li, Q. H. Li, and S. B. Yang, "Morphologies, field-emission and ultrafast nonlinear optical behavior of pure and Ag-doped ZnO nanostructures," *Journal of Alloys and Compounds*, vol. 698, pp. 284–290, 2017.

[21] D. Chu, Y. P. Zeng, and D. Jiang, "Synthesis of room-temperature ferromagnetic Co-doped ZnO nanocrystals under a high magnetic field," *Journal of Physical Chemistry C*, vol. 111, no. 16, pp. 5893–5897, 2007.

[22] H. B. Wang, F. Ma, Q. Q. Li et al., "Synthesis and stress relaxation of ZnO/Al-doped ZnO core-shell nanowires," *Nanoscale*, vol. 5, no. 7, pp. 2857–2863, 2013.

[23] Y. Chen, W. H. Tse, L. Chen, and J. Zhang, "Ag nanoparticles-decorated ZnO nanorod array on a mechanical flexible substrate with enhanced optical and antimicrobial properties," *Nanoscale Research Letters*, vol. 10, no. 1, article 712, 2015.

[24] S. Kalusniak, S. Sadofev, and F. Henneberger, "ZnO as a tunable metal: new types of surface plasmon polaritons," *Physical Review Letters*, vol. 112, no. 13, p. 137401, 2014.

[25] L. Schmidt-Mende and J. L. MacManus-Driscoll, "ZnO - nanostructures, defects, and devices," *Materials Today*, vol. 10, no. 5, pp. 40–48, 2007.

[26] S. Y. Li, C. Y. Lee, P. Lin, and T. Y. Tseng, "Gate-controlled ZnO nanowires for field-emission device application," *Journal of Vacuum Science & Technology B: Microelectronics and Nanometer Structures*, vol. 24, no. 1, pp. 147–151, 2006.

[27] S. M. Pimenov, V. D. Frolov, A. V. Kudryashov et al., "Electron field emission from semiconducting nanowires," *Diamond and Related Materials*, vol. 17, no. 4-5, pp. 758–763, 2008.

[28] S. S. Park, J. M. Lee, S. I. Yoon et al., "Low-temperature synthesis of one-dimensional ZnO nanostructures on screen- printed carbon nanotube films," *Physica E: Low-dimensional Systems and Nanostructures*, vol. 40, no. 7, pp. 2526–2530, 2008.

[29] S. H. Kim and D. G. Lee, "Effects of constituents in CNT pastes on the field emission characteristics of carbon nanotubes," *Journal of the Korean Institute of Electrical and Electronic Material Engineers*, vol. 24, no. 3, pp. 245–249, 2011.

[30] S. J. Kyung, J. B. Park, B. J. Park et al., "The effect of Ar neutral beam treatment of screen-printed carbon nanotubes for enhanced field emission," *Journal of Applied Physics*, vol. 101, no. 8, article 083305, 2007.

[31] N. Pan, H. Xue, M. Yu et al., "Tip-morphology-dependent field emission from ZnO nanorod arrays," *Nanotechnology*, vol. 21, no. 22, pp. 225707–225712, 2010.

[32] D. N. Montenegro, A. Souissi, C. Martínez-Tomás, V. Muñoz-Sanjosé, and V. Sallet, "Morphology transitions in ZnO nanorods grown by MOCVD," *Journal of Crystal Growth*, vol. 359, pp. 122–128, 2012.

[33] I. S. Cho, Z. Chen, A. J. Forman et al., "Branched TiO2Nanorods for photoelectrochemical hydrogen production," *Nano Letters*, vol. 11, no. 11, pp. 4978–4984, 2011.

[34] K. S. Ahn, Y. Yan, S. Shet, T. Deutsch, J. Turner, and M. Al-Jassim, "Enhanced photoelectrochemical responses of ZnO films through Ga and N codoping," *Applied Physics Letters*, vol. 91, no. 23, p. 231909, 2007.

[35] Y. Zang, X. He, J. Li et al., "Band edge emission enhancement by quadrupole surface plasmon–exciton coupling using direct-contact Ag/ZnO nanospheres," *Nanoscale*, vol. 5, no. 2, pp. 574–580, 2013.

[36] S. Gao, H. Zhang, R. Deng, X. Wang, D. Sun, and G. Zheng, "Engineering white light-emitting Eu-doped ZnO urchins by biopolymer-assisted hydrothermal method," *Applied Physics Letters*, vol. 89, no. 12, pp. 123125–123125, 2006.

[37] X. Yang, A. Wolcott, G. Wang et al., "Nitrogen-doped ZnO nanowire arrays for photoelectrochemical water splitting," *Nano Letters*, vol. 9, no. 6, pp. 2331–2336, 2009.

[38] A. S. M. Iftekhar Uddin and G. S. Chung, "Acetylene gas sensing properties of silver nanoparticles decorated ZnO morphologies with reduced graphene oxide hybrids," in *2015 IEEE SENSORS*, pp. 1–4, Busan, South Korea, November 2015.

[39] A. Umar, B. Karunagaran, E.-K. Suh, and Y. B. Hahn, "Structural and optical properties of single-crystalline ZnO nanorods grown on silicon by thermal evaporation," *Nanotechnology*, vol. 17, no. 16, pp. 4072–4077, 2006.

[40] L. M. Yu and C. C. Zhu, "Field emission characteristics study for ZnO/Ag and ZnO/CNTs composites produced by DC electrophoresis," *Applied Surface Science*, vol. 255, no. 20, pp. 8359–8362, 2009.

[41] S. S. Warule, N. S. Chaudhari, J. D. Ambekar, B. B. Kale, and M. A. More, "Hierarchical nanostructured ZnO with nanorods engendered to nanopencils and pin-cushion cactus with its field emission study," *ACS Applied Materials & Interfaces*, vol. 3, no. 9, pp. 3454–3462, 2011.

[42] J. Li, S. K. Cushing, P. Zheng et al., "Solar hydrogen generation by a CdS-Au-TiO_2 sandwich nanorod array enhanced with Au nanoparticle as electron relay and plasmonic photosensitizer," *American Chemical Society*, vol. 136, no. 23, pp. 8438–8449, 2014.

[43] Y. C. Pu, G. Wang, K. D. Chang et al., "Au nanostructure-decorated TiO2Nanowires exhibiting photoactivity across entire UV-visible region for photoelectrochemical water splitting," *Nano Letters*, vol. 13, no. 8, pp. 3817–3823, 2013.

[44] J. Wang, S. Pan, M. Chen, and D. A. Dixon, "Gold nanorod-enhanced light absorption and photoelectrochemical performance of α-Fe2O3Thin-Film electrode for solar water splitting," *Journal of Physical Chemistry C*, vol. 117, no. 42, pp. 22060–22068, 2013.

[45] C. Zhang, H. Y. Xu, W. Z. Liu et al., "Enhanced ultraviolet emission from Au/Ag-nanoparticles @MgO/ZnO heterostructure light-emitting diodes: a combined effect of exciton- and photon-localized surface plasmon couplings," *Optics Express*, vol. 23, no. 12, pp. 15565–15574, 2015.

[46] X. Zhang, Y. Liu, and Z. Kang, "3D branched ZnO nanowire arrays decorated with plasmonic Au nanoparticles for high-performance photoelectrochemical water splitting," *ACS Applied Materials & Interfaces*, vol. 6, no. 6, pp. 4480–4489, 2014.

[47] Q. Tao, S. Li, C. Ma, K. Liu, and Q. Y. Zhang, "A highly sensitive and recyclable SERS substrate based on Ag-nanoparticle-decorated ZnO nanoflowers in ordered arrays," *Dalton Transactions*, vol. 44, no. 7, pp. 3447–3453, 2015.

[48] Y. H. Ko and J. S. Yu, "Silver nanoparticle decorated ZnO nanorod arrays on AZO films for light absorption

enhancement," *Physica Status Solidi A*, vol. 209, no. 2, pp. 297–301, 2012.

[49] C.-C. Yang, H.-C. Yu, Y.-K. Su, M.-Y. Chuang, C.-H. Hsiao, and T.-H. Kao, "Noise properties of Ag nanoparticle-decorated ZnO nanorod UV photodetectors," *IEEE Photonics Technology Letters*, vol. 28, no. 4, pp. 379–382, 2016.

[50] F. Li, S. Wu, L. Zhang, and Z. Li, "Ag nanoparticles decorated ZnO nanoarrays with enhanced surface-enhanced Raman scattering and field emission property," *Journal of Materials Science: Materials in Electronics*, vol. 28, no. 21, pp. 16233–16238, 2017.

[51] X. Dong, P. Yang, C. Jia, F. Yang, and D. Wang, "Ag nanoparticle-decorated ZnO nanorod arrays: synthesis, growth mechanism, and properties," *Nanoscience and Nanotechnology Letters*, vol. 6, no. 8, pp. 711–716, 2014.

[52] Q. Deng, X. Duan, D. H. L. Ng et al., "Ag nanoparticle decorated nanoporous ZnO microrods and their enhanced photocatalytic activities," *ACS Applied Materials & Interfaces*, vol. 4, no. 11, pp. 6030–6037, 2012.

[53] W. Z. Liu, H. Y. Xu, C. L. Wang et al., "Enhanced ultraviolet emission and improved spatial distribution uniformity of ZnO nanorod array light-emitting diodes via Ag nanoparticles decoration," *Nanoscale*, vol. 5, no. 18, pp. 8634–8639, 2013.

[54] K.-X. Zhang, C.-B. Yao, X. Wen, Q.-H. Li, and W.-J. Sun, "Ultrafast nonlinear optical properties and carrier dynamics of silver nanoparticle-decorated ZnO nanowires," *RSC Advances*, vol. 8, no. 46, pp. 26133–26143, 2018.

[55] K.-X. Zhang, X. Wen, C.-B. Yao et al., "Synthesis, structural and optical properties of silver nanoparticles uniformly decorated ZnO nanowires," *Chemical Physics Letters*, vol. 698, pp. 147–151, 2018.

[56] N. L. Tarwal and P. S. Patil, "Enhanced photoelectrochemical performance of Ag-ZnO thin films synthesized by spray pyrolysis technique," *Electrochimica Acta*, vol. 56, no. 18, pp. 6510–6516, 2011.

[57] K. S. Ahn, S. Shet, T. Deutsch et al., "Enhancement of photoelectrochemical response by aligned nanorods in ZnO thin films," *Journal of Power Sources*, vol. 176, no. 1, pp. 387–392, 2008.

[58] S. Shet, "Zinc oxide (ZnO) nanostructures for photoelectrochemical water splitting application," *ECS Transactions*, vol. 33, no. 38, pp. 15–25, 2011.

[59] A. Wolcott, W. A. Smith, T. R. Kuykendall, Y. Zhao, and J. Z. Zhang, "Photoelectrochemical study of nanostructured ZnO thin films for hydrogen generation from water splitting," *Advanced Functional Materials*, vol. 19, no. 12, pp. 1849–1856, 2009.

Hindawi
Journal of Nanomaterials
Volume 2020, Article ID 6185976, 10 pages
https://doi.org/10.1155/2020/6185976

Research Article

Investigating Methylene Blue Adsorption and Photocatalytic Activity of ZnO/CNC Nanohybrids

Vu Nang An,[1,2] Tran T. T. Van,[1,2] Ha T. C. Nhan,[1,2] and Le Van Hieu[1,2,3]

[1]*Faculty of Materials Science and Technology, University of Science, VNU–HCM, Vietnam*
[2]*Vietnam National University Ho Chi Minh City, Vietnam*
[3]*Laboratory of Multifunctional Materials, University of Science, VNU–HCM, Vietnam*

Correspondence should be addressed to Le Van Hieu; lvhieu@hcmus.edu.vn

Received 27 December 2019; Revised 13 February 2020; Accepted 28 February 2020; Published 17 March 2020

Guest Editor: Ana C. S. Alcântara

Nanohybrids of zinc oxide/cellulose nanocrystals (ZnO/CNCs) were successfully prepared by using a low cost and green method for adsorption and photocatalytic degradation of methylene blue (MB). CNCs have been derived through the hydrolysis reaction by citric/hydrochloric acid from the pure cellulose isolated from Vietnamese *Nypa fruticans* trunk. The influence of the Zn^{2+} ion concentration on the morphology, microstructure, and thermal properties as well as the photocatalytic activity of the ZnO/CNC nanohybrids was investigated in detail. Analyses of FTIR spectra, XRD, and SEM indicated that the ZnO nanocrystals with the size of 50 nm formed and loaded on the surface of CNC. Based on the DRS spectra and the nitrogen adsorption–desorption isotherms (BET) analysis, the absorption of ultraviolet light with a strong absorption band around 400 nm was found for all the ZnO/CNC nanohybrids, and the values of specific surface areas (S_{BET}) of materials can be controlled by changing the concentration ratio of Zn^{2+} ion and CNC. The TGA analysis demonstrated that the ZnO loading samples (ZnO/CNC) had the thermal degradation onset temperature higher than that of neat CNC. The effect of MB removal showed the results which were contributed not only by the adsorption ability of CNC but also by the photocatalytic activity of ZnO. The photocatalytic efficiency significantly depended on the content of ZnO loading. The maximum degradation of MB was about 95% in 150 min for the ZnO/CNC-1.0 sample in which the concentration ratio of zinc-precursor $Zn(NO_3)_2{\cdot}6H_2O$ and CNC was 1.0.

1. Introduction

Cellulose as one of the most abundant natural biopolymers has been widely used as a reinforcing material for fiber–thermoplastic composite materials [1–5]. Cellulose nanocrystals (CNCs) prepared by acid hydrolysis of natural cellulose are typically formed of a rigid rod-shaped monocrystalline domain at different nanosizes of 1–100 nm (in diameter), depending on the biomass source [6]. CNCs have been using as nanofillers in polymer composites, in food and cosmetics, etc. [7, 8]. CNCs have many advantage aspects such as excellent mechanical properties, high aspect ratio, nanoscale dimension, low cost, availability, and renewability [9]. However, monofunctional CNC can be only applied in various biomedical and photocatalytic fields since many researchers are trying to make its more functionalization such as chemical modification and doping with other nanomaterials.

ZnO nanoparticles (ZnO NPs) were reported to have the notable optoelectronic properties, high catalytic activity for chemical and biological species, and strong antimicrobial properties for wide range of pathogens [10]. Having the band gap of ZnO of 3.3 eV similar to that of TiO_2 (3.2 eV for anatase), the ZnO shows the also remarkable optical and photocatalytical properties. Therefore, ZnO was also found in many applications in functional optical devices, ultraviolet photodetectors, gas sensors, solar cells, ultraviolet laser diodes, and ion insertion batteries [11–14] and also in medical and pharmaceutical industries for drug delivery and cosmetics manufacturing. In other hand, one of attracting recent development of ZnO application in waste water treatment is for the degradation of pollutants including organic dyes,

effluents, and also for the removal of heavy metals during waste water purification [15–17]. However, ZnO nanoparticles tend to aggregate due to their large surface area and high surface energy. To overtake this problem and improve nanoscale dispersion, the fabrication of ZnO nanoparticles in using the nanofibrillar materials (such as cellulose and its derivatives) as a substrate has attracted attention for many potential applications in different areas. Although the research on cellulose-based nanocomposites is continuously growing, there are few studies published on the synthesis of ZnO NPs on the cellulose substrate. These studies reported the complicated preparation methods and take a longtime process of experiment, which are not efficient for industrial application. For example, Ul-Islam et al. [18] have used three time-experimental steps to prepare ZnO/CNC nanohybrids by using regenerated bacterial cellulose (RBC) templates. The obtained nanohybrids showed efficient antibacterial properties, but the degradation temperatures were increased slightly by 5–10°C compared with neat RBC. More recently, a two-step preparation method for ZnO/CNC nanohybrids was reported. The first step is the preparation of CNC using hydrochloric acid hydrolysis and then the next is the formation of ZnO nanoparticles on the surface of the CNC using a precipitation method. This result was shown the relatively weak interactions between the CNC and ZnO nanoparticles due to the weak electrostatic interactions between the hydroxyl groups on the surface of the CNC and the Zn^{2+} [19, 20]. The achieved ZnO/CNC nanohybrids exhibited stronger antibacterial activity than the CNC ions. In this work, a simple, green one-step synthesis technique was applied to fabricate ZnO/CNC hybrids at mild temperature of 80°C in using solely water solvent and especially Vietnamese biosource *Nypa fruticans* cellulose nanocrystals which were used as the biotemplate in order to improve the adsorption and photocatalytic efficiency of ZnO NPs. Moreover, the morphology, structure, and properties of the ZnO/CNC nanohybrids were investigated with different ratios. This method could be used as one of the approaches for the development of cheaper and more effective technologies for industrial wastewater purification.

2. Materials and Methods

Nypa Fruticans trunk (NFT) was collected from muddy areas along the riverside in Ben Tre, Southwest of Vietnam. Zinc nitrate ($Zn(NO_3)_2.6H_2O$, 98%) and sodium hydroxide (NaOH, 96%) were purchased from Guangdong Guanghua Sci-Tech Co., Ltd., China. Formic acid (HCOOH, 90%), hydrogen peroxide (H_2O_2, 30%), and sulfuric acid (H_2SO_4, 98%) were procured from Xilong Scientific Co., Ltd., China.

2.1. Extraction of Cellulose from NFT. Cellulose was isolated from NFT as raw material by chemical treatment method [21]. First, the raw cellulose bulk of NFT was peeled off and cut into chunks around 30 cm in length and 1 cm^2 of edge surface area. These chunks of NFT had been then laminated by a rolling machine before dried and splitted into fibers. Then, they were grinded into fine powder and stirred well in 1000 mL of distilled water at 100°C for 2 h to remove impurities and aqueous soluble organic substances. They were then cooled to room temperature and filtered. This process was conducted twice, and the final bulk celluloses were then dried in an air oven at 70°C for 8 h. Twenty grams of the pretreated biomass powder were dispersed into HCOOH 90% (1 : 10 w/v) solution at 100°C for 2 h by magnetic agitator in circulation system. This suspension was filtered, and the obtained residue was washed successively with pure HCOOH acid and warm distilled water to break the β-O-4 linkages of hemicellulose as well as dissolve the impurities remnant. To remove hemicellulose, after pretreatment with acid, samples were dissolved into PFA (a mixed solvent of formic acid, hydrogen peroxide, and distilled water with the ratio of 90 : 4 : 6% *w*/*w*, respectively) and stirred well at 80°C for 2 h. The suspension was then filtered and washed with formic acid (80%) and distilled water, respectively. Finally, the fiber was bleached with a combined solution of NaOH and H_2O_2 (1 : 1 *w*/*w*) in using a magnetic stirring circulation system at 80°C for 1 h, finally filtered and rinsed several times to get rid of lignin and hemicelluloses. This bleaching process was repeated two times until the fibers became white. It has been reported that apart from improving the physical appearance of fibers, bleaching procedure also helps in improvement of mechanical properties due to the better interfacial adhesion between fibers and matrix [22]. The cellulose was then obtained after filtration and three times washing with deionized water and allowed to air dry for 48 h.

2.2. Preparation of Zinc Oxide/Cellulose Nanocrystal (ZnO/CNC) Nanohybrids. ZnO/CNC nanohybrids were prepared by a one-pot synthesis route as reported in other paper [23] in which CNC with carboxyl groups was obtained to fabricate $Zn(OH)_2$/CNC by simple precipitation through electrostatic interaction, and finally, ZnO/CNC nanohybrids were achieved by thermal treatment. In our experiment, the starting cellulose (8 g) was added to 400 mL mixed acid solution of 90% $C_6H_8O_7$/10% HCl (400 mL, 3 M $C_6H_8O_7$, and 6 M HCl). The mixture was heated at 80°C for 6 h under continuously mechanical stirring, and the suspension was rapidly cooled to room temperature. The functionalized CNC and recycled acid mixtures were then separated by filtration processes, and the CNC samples were washed 3 times with deionized water by centrifugation. The centrifuged samples were left overnight by drying in an oven at 80°C for several hours. This CNC powders were used directly to prepare ZnO/CNC nanohybrids by adding it to $Zn(NO_3)_2.6H_2O$ solutions (0.1 mol/L) with different weight ratios ($Zn(NO_3)_2.6H_2O$/CNC powder) of 0.5, 1.0, and 2.0. The pH values of these three samples were adjusted to 7 by using NaOH solution (0.5 mol/L). Then, the mixture was heated to 80°C, and 0.1 M NaOH solution was added dropwise to precipitate Zn^{2+} completely with vigorous stirring. $Zn(OH)_2$ nanoparticles were obtained by simple precipitation through electrostatic adsorption between carboxylates (COO^-) of CNC and Zn^{2+}. The mixture was then washed repeatedly by centrifugation (5,000 rpm for 20 min) with deionized water to remove remaining zinc species and by products. Finally, the samples were dried at 120°C for 1 h to transform $Zn(OH)_2$ to ZnO. In the following manuscript, the three samples were labelled

according to the weight ratio of $Zn(NO_3)_2.6H_2O$ to CNC powder as ZnO/CNC-0.5, ZnO/CNC-1.0, and ZnO/CNC-2.0. For reference, the as-produced CNC suspensions were also purified by deionized water to remove the remaining cellulose hydrolysis products.

2.3. Characterization. The structure morphologies of the CNC and ZnO/CNC nanohybrids were observed at room temperature by using the field-emission scanning electron microscopy (FE-SEM, S-4800; Hitachi, Japan) at acceleration voltage of 10.0 kV. Fourier-transform infrared (FT-IR) spectra of the samples were obtained by using an FT-IR spectrometer (Nicolet 6700; Thermo Fisher SCIENTIFIC, USA) using the KBr disc method. Disks containing 2 mg of sample were scanned in the wavenumber range of 400-4,000 cm^{-1}. The crystalline phase and its crystallite size of synthesized CNC powders and ZnO/CNC nanohybrids were characterized by an X-ray powder diffractometer (XRD, D2 PHASER; Bruker) with monochromatic Cu K_α radiation at $\lambda = 1.54056$ Å in the 2θ range of 10–80° at scan rate of 0.02°/min. The X-ray generator tension and current were 40 kV and 30 mA, respectively. The TGA experiment was conducted using a thermogravimetric analyzer (TA Instruments TGA Q500). The samples (15–20 mg) were heated at a rate of 10°C/min from room temperature to 700°C under a nitrogen flow rate of 30 mL·min^{-1}. The specific surface area of our materials was measured via the nitrogen adsorption–desorption experiments on a NOVA 1000e analyzer (Quantachrome Instruments). The band gap energy (Eg) values of nanohybrids were determined from room temperature UV-visible diffuse reflectance spectra (DRS) using a Perkin-Elmer Lambda 850 Spectrophotometer equipped with a 15 cm diameter integrating sphere bearing the holder in the bottom horizontal position.

2.4. Adsorption and Photocatalytic Evaluation. The adsorption/photocatalytic efficiency of the samples was investigated by monitoring the removal of MB dye as a model compound. 40 mg of ZnO/CNC powders were dispersed into 50 mL of MB aqueous solution (10.0×10^{-5} M). In order to determine adsorption equilibrium, the suspensions were stirred in dark for 2.5 h at 200 rpm. The saturation adsorption was obtained after 15 min. Continuously, the suspensions were irradiated by UVC lamp (15 W Osram Germicidal, $\lambda = 234$ nm) to activate the photocatalytic process. A certain amount of solution (~3 mL) was taken out at given time intervals (30 min), and a UV–vis spectrophotometer (model V-670, Jasco, Japan) was used to measure the absorbance of samples. The removal percentages (R) of MB, indicating adsorption ability, were calculated by using

$$R = \frac{C_0 - C_t}{C_0} \times 100\%, \quad (1)$$

where C_o and C_t are the initial concentration and concentration of MB dye after the adsorption equilibrium without UVC irradiation, respectively. The degradation rate was calculated as follows:

$$\text{Degradation rate } (\%) = \frac{C_o - C_t}{C_t} \times 100, \quad (2)$$

where C_o represents the initial concentration of MB dye (after the absorption equilibrium) and C_t is the final concentration after illumination by UVC for t time.

3. Results and Discussion

3.1. Structure, Morphology, and Surface Area of CNC and ZnO/CNC Nanohybrids

3.1.1. Structure. The XRD diffractograms of every NFT treatment stage and the CNC, ZnO, and ZnO/CNC-0.5 nanohybrids are shown in Figure 1. The results present their CNC monoclinic structure. The (101), (002), and (040) lattice planes were observed at $2\theta = 16.15$, 22.65, and 34.88°, respectively. These peaks correspond to polymorph of cellulose I (indexed to the database of ID number COD 4114994) [24]. XRD profiles of the cellulosic products obtained at each stage were analyzed to monitor the evolution of the percentage crystalline index (CrI) of nanocellulose. The physical and mechanical properties of cellulose are influenced by its crystalline structure. CrI is one important parameter of the crystal structure. The pretreatment of cellulose fibers increases their CrI meaning to the increasing of ratio of crystalline and amorphous region and surface roughness as well. This made it easy for the adhesion of ZnO onto the cellulose matrix. From XRD analysis, the CrI of cellulose and pretreated fibers was calculated in using the amorphous subtraction method described by Equation (3) [25]:

$$\text{CrI } (\%) = \frac{I_{002} - I_{\text{am}}}{I_{002}} \times 100, \quad (3)$$

where I_{002} is the maximum diffraction intensity of the characteristic peak (002) at around 22–23° and I_{am} is the diffraction intensity attributed to amorphous cellulose, which is the valley between peaks (101) and (002). Treatment of the fibers increased their % CrI. The calculated % CrI were 57.1, 62.3, 78.9, and 84.5% for biomass obtained after acid, PFA, bleaching treatments, and the final acid hydrolysis, respectively. From these results, it can be deduced that each treatment step affected the crystallinity of the materials. The CrI was found to have increased by 26.9% after the removal of lignin and hemicellulose. The increasing % CrI indicates an improvement of the cellulose crystallinity.

The XRD patterns of ZnO with high intensity of the peaks revealed the single-phase crystalline nature of the synthesized ZnO nanostructures. The characteristic peaks correspond to the (100), (002), (101), (102), (110), (103), (200), (201), and (112) planes of ZnO were observed at $2\theta = 31.89$, 34.60, 36.39, 47.62, 56.67, 62.97, 66.47, 68.11, and 69.17°, respectively. This result is similar to those reported previously [16, 17] and are consistent with the database of ID number COD 1011258 with a wurtzite hexagonal crystallographic lattice of ZnO. The ZnO/CNC-0.5 XRD profile displays two-phase structures corresponding to cellulose (∗) and ZnO (#) as indicated in Figure 1(b). In addition, the XRD

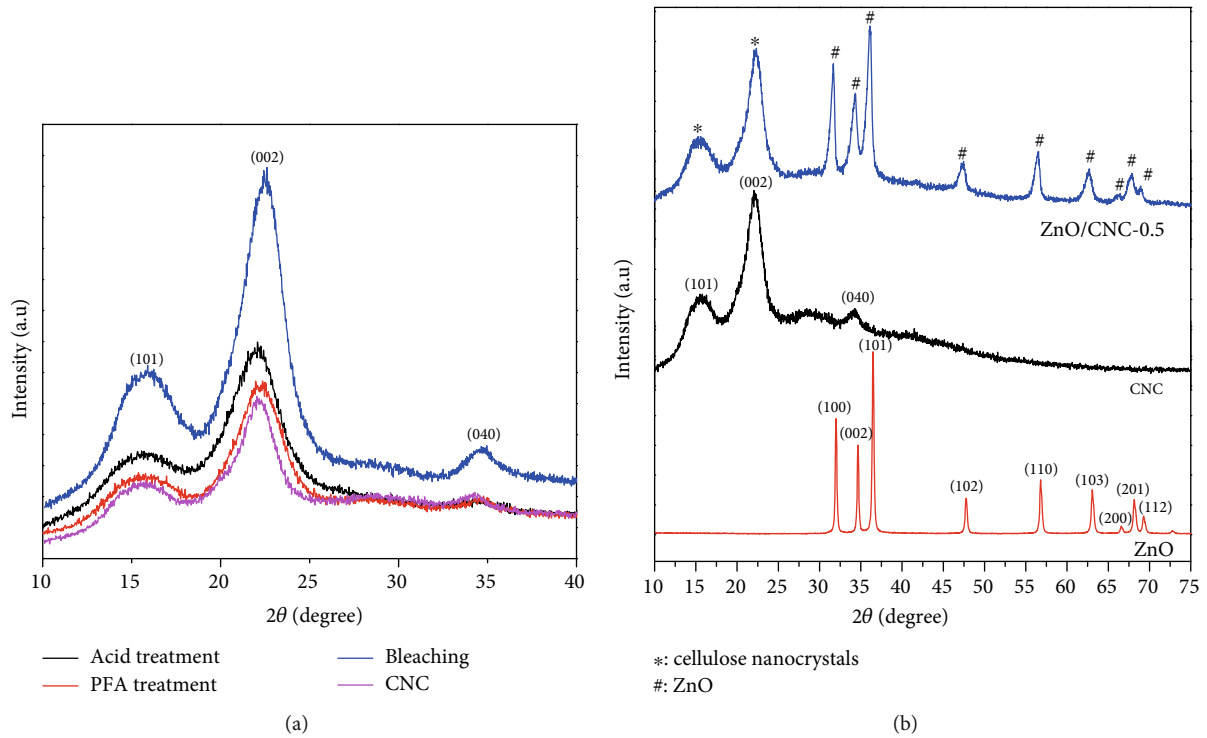

Figure 1: XRD patterns of different treatment stages by acid, PFA, bleaching, and the final acid hydrolysis for NFT (a) and CNC, ZnO, and ZnO/CNC-0.5 nanohybrids (b).

diagrams of ZnO/CNC-1.0 and ZnO/CNC-2.0 nanohybrids were similar to that of ZnO/CNC-0.5 in Figure 2, indicating the successful synthesis of this material by the facile one-step route. It can be deduced from these profiles that the presence of well crystalline ZnO has not altered the crystal structure of the cellulose matrix.

The average crystallite size (D) of cellulose, pure ZnO, and ZnO in the nanohybrids was calculated from XRD analysis using Equation (4): the Debye-Scherrer formula:

$$D = \frac{0.9\lambda}{\beta \cos\theta}, \tag{4}$$

where D is the crystallite size corresponding to the (hkl) plane, λ is the wavelength of copper K_α X-ray radiation (1.5406 Å), β is the observed angular width at half maximum intensity (FWHM), and θ is the Bragg diffraction angle measured in radians. In this work, the most intense diffraction lines ((100), (002), and (101)) were selected to calculate the average size of ZnO crystals. The lattice parameters a, b, and c, which are related to the interplanar distance (d) and Miller indices h, k, and l, were calculated for pure ZnO and ZnO in the nanohybrids using Equation (5) to determine the influence of cellulose nanocrystals

$$\frac{1}{d^2} = \frac{4}{3}\left(\frac{h^2 + hk + l^2}{a^2}\right) + \frac{l^2}{c^2}. \tag{5}$$

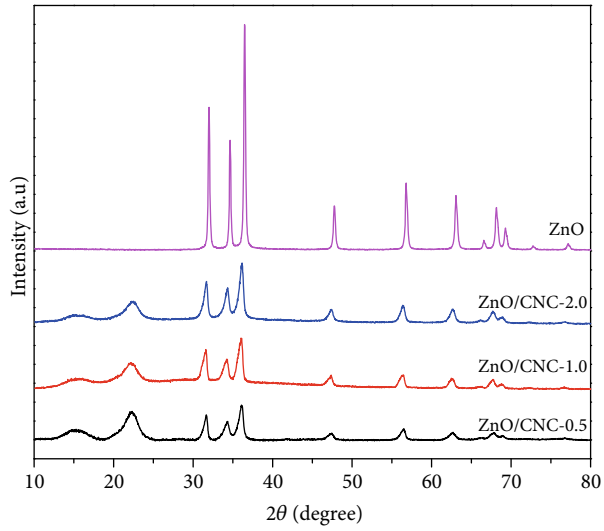

Figure 2: XRD patterns of ZnO and ZnO/CNC nanohybrids.

The calculated lattice parameters are reported in Table 1. As observed in literature [22], compared to pure ZnO, the crystallite size of ZnO in the nanohybrids is much smaller, and there is a slight increase in the value of lattice parameters. According to Sharma et al. [26], the increase in the value of lattice parameters indicates the stretching of unit cells due to adsorption of polymer molecular chains on the surface of ZnO nanostructures.

The chemical structure of CNC and ZnO/CNC nanohybrids was analyzed using FTIR spectroscopy as shown in Figure 3. Similar characteristic bands corresponding to CNC

Table 1: Structural parameters of ZnO nanocrystals.

Sample	Crystallite size (nm)	Interplanar distance (d) (nm)	Lattice parameters		Lattice constant c/a
			$a = b$ (nm)	c (nm)	
ZnO (pure)	32.8	0.2461	0.5323	0.2833	0.5323
ZnO/CNC-0.5	6.8	0.2489	0.5359	0.2872	0.5359
ZnO/CNC-1.0	9.1	0.2498	0.5369	0.2883	0.5369
ZnO/CNC-2.0	10.3	0.2489	0.5359	0.2872	0.5359

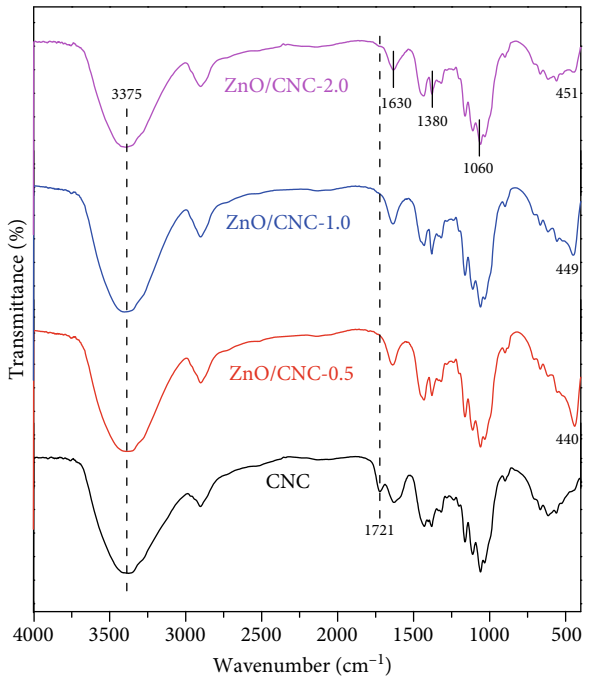

Figure 3: FT-IR spectra of CNC and ZnO/CNC nanohybrids.

were observed for the ZnO/CNC nanohybrids at 3,375 and 1,380 cm^{-1}, which can be related to stretching and bending vibrations of hydroxyl groups, respectively. The peaks at around 1,630 and 1,060 cm^{-1} can be attributed to O–H bending of absorbed water and C–O–C stretching of pyranose and glucose ring skeletal vibration, respectively.

Compared to CNC, the nanocrystalline character of the obtained ZnO nanoparticles in the nanohybrids was confirmed by a new absorption band at 440 cm^{-1}, assigned to Zn–O stretching vibration. With increasing concentration of Zn^{2+} ions, a slight shift of the Zn–O stretching bands to higher wavenumber was observed due to the lattice parameter of the ZnO nanoparticles. Besides, in comparison to CNC, the band intensity of C=O stretching vibration (1,721 cm^{-1}) decreased, which was ascribed to strong interactions between oxygen atoms of carboxyl groups on the surface of the CNC and ZnO nanoparticles.

The DRS curves of the ZnO and ZnO/CNC nanohybrids are presented in Figure 4(a). The figure shows the strong absorption edge around 400 nm for all the ZnO/CNC nanohybrids. Based on the Tauc plot in Figure 4(b), the band gap values of them range about 3.1-3.2 eV. This result implies that these materials could absorb the irradiation light at wavelength of 254 nm in photocatalysis process.

3.1.2. Morphology and Surface Area. FE-SEM images of the CNC and ZnO/CNC nanohybrids are shown in Figure 5. It can be observed that the CNC appeared as rod-like monocrystals of 20 nm in diameter and 240–300 nm in length. After the precipitation process between CNC and Zn^{2+} ions, well-dispersed ZnO nanoparticles with average diameter of 50.2 nm and narrow size distribution (15–85 nm) were anchored on the surface of the CNC (ZnO/CNC-1.0). With increasing concentration of Zn^{2+} ions, the average diameter of the ZnO nanoparticles increased to 126.6 nm in ZnO/CNC-2.0.

The increase of Zn^{2+} ion concentration on the surface of the CNC enhances more Zn^{2+} ions anchored on CNC. This leads to an increase of ZnO particles not only in number but also in size on the surface of the CNC.

The formation of ZnO on CNC can be explained as follows. During the CNC hydrolysis, the hydronium ions (H_3O^+) from HCl catalysts were used to catalyze the esterification of hydroxyl groups on the exposed cellulose chains with carboxyl groups of citric acid ($C_6H_8O_7$). This reaction leads to the existence of carboxyl groups (–COOH) on the surface of citrate CNC. Then, $Zn(NO_3)_2.6H_2O$ solutions were added, and Zn^{2+} ions would be adsorbed on COO^- negative site CNC surface due to the strong electrostatic interactions of these ions. When the Zn^{2+} concentration was low, the concentration of the carboxylate anion (COO^-) from carboxyl groups on the CNC template was high. All Zn^{2+} ions were significantly located at these negative site, bonded to the anionic OH^- to form the monomer zinc hydroxide $Zn(OH)_2$ and two adjacent $Zn(OH)_2$ dehydrated to form zinc oxide (ZnO) particles. As the result, the growth of ZnO crystals on CNC surface deduces an increase of the surface area. Figure 6 shows the nitrogen adsorption–desorption isotherms and the values of specific surface areas (S_{BET}) of samples with different concentrations of ZnO.

At light zinc-precursor $Zn(NO_3)_2.6H_2O$, the synthesized nanohybrids showed an increased surface area compared with CNC. The S_{BET} values of the CNC, ZnO/CNC-0.5, and ZnO/CNC-1.0 were 69.1, 73.1, and 74.8 $m^2 \cdot g^{-1}$, respectively.

As the Zn^{2+} concentration increased, there are a large amount of $Zn(OH)_2$ monomers formed in bulk solution, not anchored on the surface of the CNC. After that, the new bonds are produced after two $Zn(OH)_2$ monomer dehydration to assemble along a certain orientation direction. The ZnO crystals grew continuously and eventually formed a sheet-like structure with the average diameter of the ZnO nanoparticles increased to 126.6 nm diameter, as show in FESEM image of ZnO/CNC-2.0 nanohybrid. The assembly of ZnO nanoparticles into two-dimensional sheet-like structure of CNC

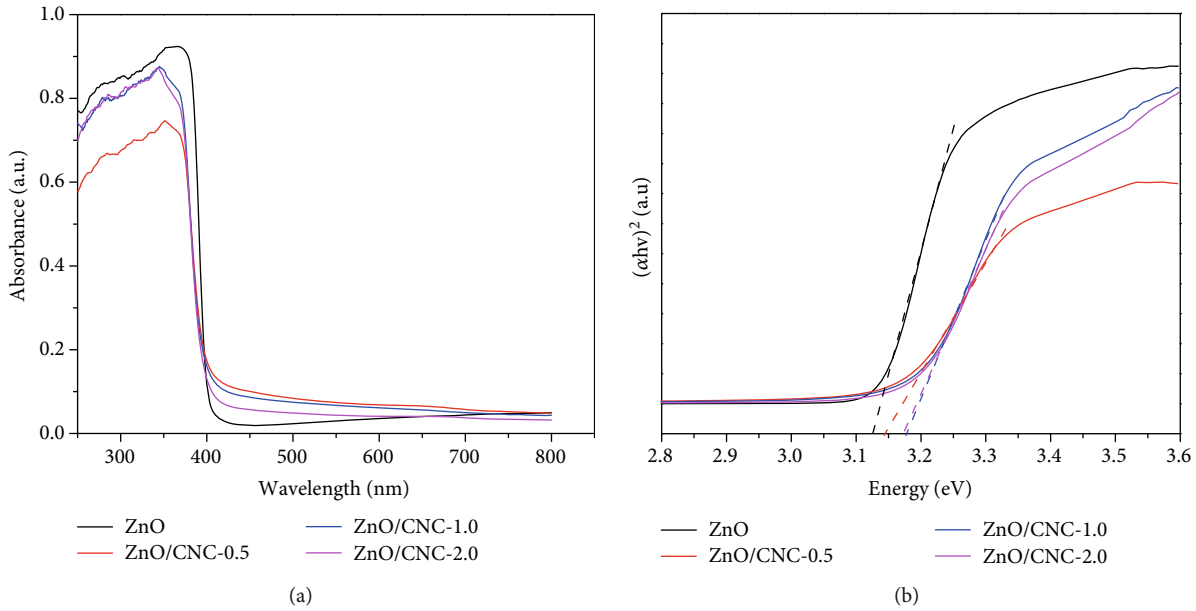

Figure 4: UV-vis diffuse reflectance spectra (a) and band gap determination from Tauc plot (b) of ZnO and nanohybrids.

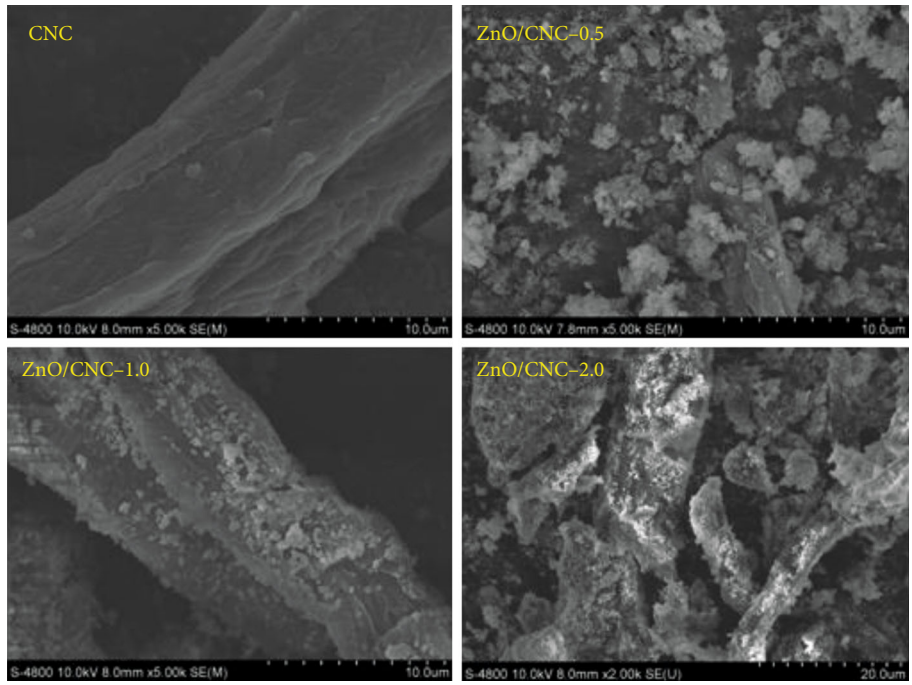

Figure 5: FE-SEM images of CNC and ZnO/CNC nanohybrids.

template led to a decrease of surface area as indicated in BET results of ZnO/CNC-2.0 nanohybrid (Figure 6).

3.2. Thermal Properties of CNC and ZnO/CNC Nanohybrids. Thermogravimetric analysis (TGA) has been used to characterize the thermal behavior of the CNC and ZnO/CNC nanohybrids. The thermal degradation onset temperature (T_o), maximum degradation temperature (T_{max}), and apparent activation energy (E_a) are listed in Table 2.

Figure 7 shows the thermal degradation of CNC and ZnO/CNC nanohybrids elaborated by the one main step of maximum degradation temperature. It shows that the CNC has the lowest thermal stability (Figure 7(a)). The T_o and T_{max} values of the CNC were about 293.3 and 376.7°C, respectively. Thermal degradation of cellulose involves depolymerization, dehydration, and decomposition of glycosyl units followed by formation of a charred residue. The result indicates that inorganic nanomaterials can significantly improve the thermal stability of polymer matrix. In comparison to CNC, the thermal degradation curves of the ZnO/CNC nanohybrids with a single degradation peak have shifted to higher temperature (Figure 7(b)). Furthermore, the T_o and

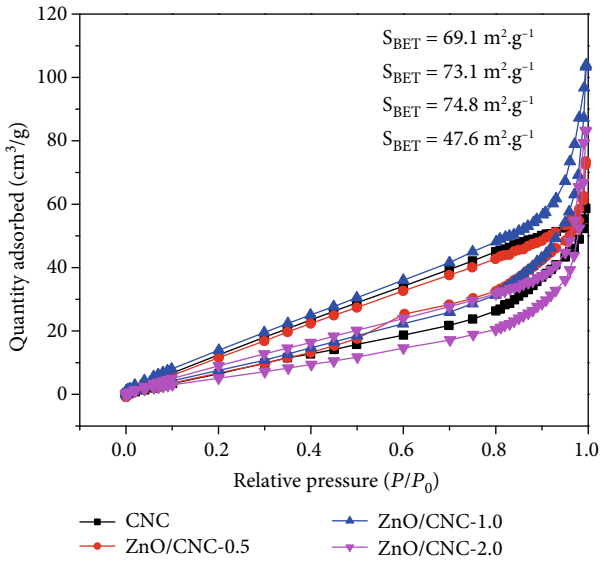

Figure 6: Nitrogen adsorption–desorption isotherm curves for CNC, ZnO/CNC-0.5, ZnO/CNC-1.0, and ZnO/CNC-2.0 nanohybrids.

Table 2: T_o, T_{max}, and E_a parameters for CNC and ZnO/CNC nanohybrids.

Sample	T_o (°C)[a]	T_{max} (°C)[a]	E_a (kJ·Mol^{-1})[b]
CNC	293.3	376.7	128.7
ZnO/CNC-0.5	327.7	367.7	117.7
ZnO/CNC-1.0	329.5	373.6	137.7
ZnO/CNC-2.0	321.6	357.4	176.0

[a]T_o and T_{max} calculated from TGA curves. [b]E_a calculated by the Horowitz and Metzger method.

T_{max} values increased to 327.7 and 367.7°C for ZnO/CNC-0.5, 329.5 and 373.6°C for ZnO/CNC-1.0, and 321.6 and 357.4°C for ZnO/CNC-2.0. In particular, ZnO/CNC-1.0 showed the best thermal stability, with the increase of T_o (36.2°C) as compared to neat CNC. This was ascribed to the stronger interactions between oxygen atoms of the CNC and ZnO nanoparticles, thus providing a thermal barrier for the cellulose skeleton. Besides, there was no further decomposition of ZnO nanoparticles after cellulose degradation, whereas an increase in the char fraction was observed for the ZnO/CNC nanohybrids (Figure 7(a)). This indicates that thermally stable inorganic ZnO nanoparticles can act as a barrier flame retardant for the cellulose skeleton based on heat absorbance, resulting the higher degradation temperature and increased weight residue.

The apparent activation energy (E_a), corresponding to interaction between CNC and ZnO nanoparticles, was calculated from the TGA data by using the Horowitz and Metzger method [27] as follows:

$$\ln\left[\ln\left(\frac{W_o}{W_T}\right)\right] = \frac{E_a\theta}{RT_S^2}, \quad (6)$$

where W_o is the initial sample weight, W_T is the residual sample weight at temperature T, T_S is the temperature determined at 36.79% weight loss, θ is $T - T_S$, and R is the gas constant.

Figure 8 shows the plots of ln [ln (W_o/W_T)] versus θ for the main stage of the thermal degradation of the CNC and ZnO/CNC, where E_a can be calculated from the slopes of the fit lines, and the results are listed in Table 2. In general, with the higher E_a value, the faster degradation rate occurs [27]. Table 2 illustrates that ZnO/CNC-2.0 showed the highest E_a value comparing to that of CNC and the other nanohybrids. Based on above results, this can be seen that the addition of ZnO nanoparticles to CNC matrix may lead to the degradation behavior of CNC in two opposite ways. On the one hand, during degradation of CNC, ZnO nanoparticles enhance the thermal stability of materials, so that the onset degradation temperature of the CNC gets higher, which is the factor resulting in increasing degradation rate of CNC. On the other hand, having strong interaction between ZnO nanoparticles with carboxyl groups of CNC, the thermally stable ZnO nanoparticles, as a flame retardant, will cover the surface of CNC and increase the CNC thermal degradation temperature.

3.3. Adsorption and Photocatalytic Properties

3.3.1. Adsorption. Because CNC surface has negative charges originating from its abundant carboxyl groups, the cationic MB molecules are adsorbed on the anionic CNC in the mixture through electrostatic interactions. This is the reason why the CNC has high adsorption ability in the dark. The MB adsorption results in Figure 9 show a comparison of dye removal ability of CNC and ZnO/CNC nanohybrids. The dye removal ability of 40.22% and 28.15% for ZnO/CNC-1.0 and ZnO/CNC-2.0, respectively, was lower than that of CNC. Meanwhile, ZnO/CNC-0.5 gave the best adsorption of dye removal (73.62%), which is higher than that of CNC. At the same time, the dye removal ability of the nanohybrids decreased with the increase of ZnO, indicating the more ZnO contents on CNC and the weaker dye absorption ability. It can be explained that since the low content of ZnO in ZnO/CNC-0.5 will make the CNC surface more roughness, creating the high specific surface area of the material leads to the enhancement of MB adsorption ability (73.62%). With the light increase of ZnO content in ZnO/CNC-1.0 and ZnO/CNC-2.0 samples, the nanoparticles were found to be well dispersed and cover the CNC surface and effect negatively the adsorption ability (40.22% and 28.15%) by hindering the interaction between MB and CNC carboxyl groups.

3.3.2. Photocatalyst. The results for the photocatalytic activity are shown in Figure 10. It can be seen that the ZnO/CNC nanohybrids possessed photocatalytic activity to decompose the dye under UV irradiation. If there was no presence of ZnO, no remarkable change in UV absorption band of MB during 1.0 h of UV irradiation was observed and then after 2.5 h UV exposure, only 2% degradation of MB has occurred. As shown in Figure 10, under UV irradiation, about 95% of

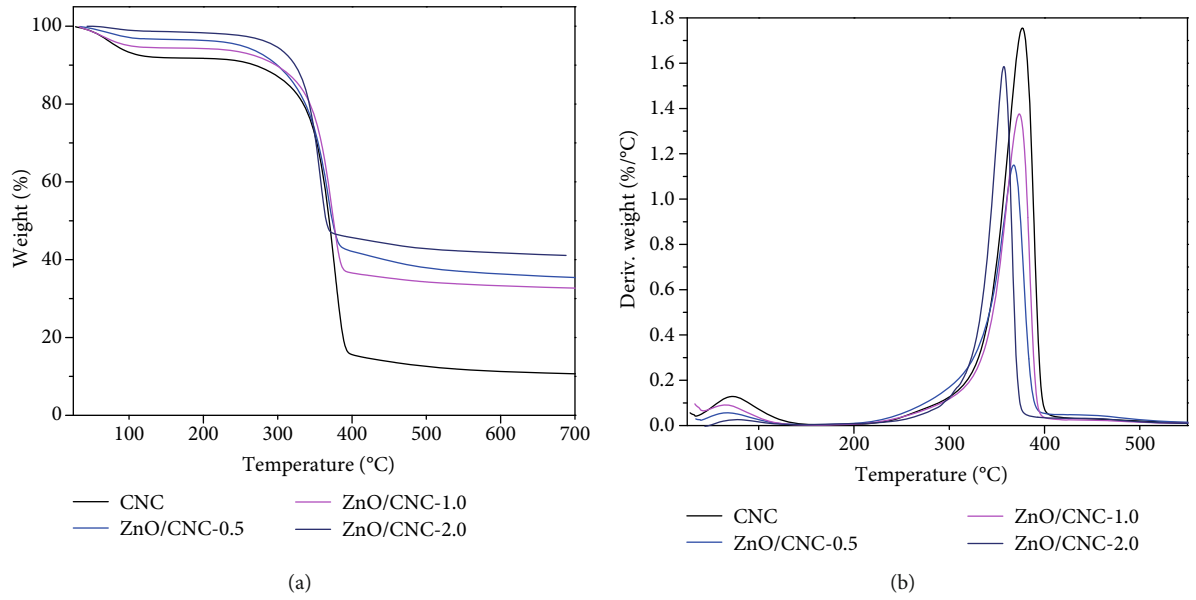

Figure 7: TGA (a) and differential thermogravimetry (DTG) (b) curves for CNC and ZnO/CNC nanohybrids.

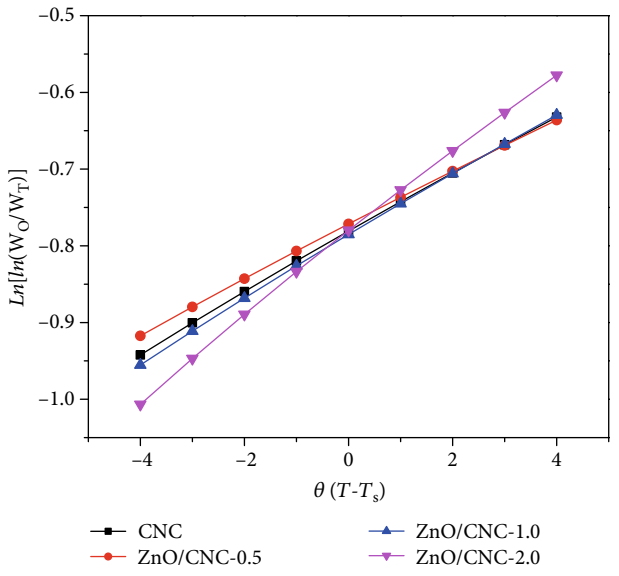

Figure 8: Plot of ln [ln (W_o/W_T)] versus θ for the main stage of thermal degradation of CNC and ZnO/CNC nanohybrids.

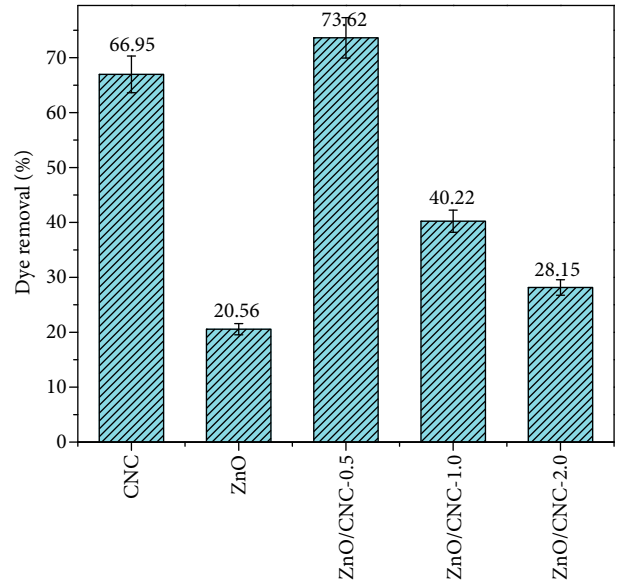

Figure 9: Dye removal of CNC and ZnO/CNC hybrids.

the MB dye was decomposed fast after irradiation during 150 min in ZnO/CNC-1.0 nanohybrid. This observation indicates that the ZnO/CNC-1.0 nanohybrid, having well dispersion at small size of ZnO nanoparticles on the CNC surface, possessed high photocatalytic activity due to the strong electronic interaction between the CNC and ZnO nanoparticles. Photocatalysis occurs as ZnO photocatalyst is irradiated by light with energy larger than its band gap energy. After absorbing excited energy, photogenerated electron–hole pairs would be produced and migrated to the surface of ZnO nanoparticles (Equation (7)). Then, these e^- and h^+ can react with O_2 and H_2O absorbed on its surface to generate active radical OH^- (Equation (8)) and O_2^- (Equation (9)), which could participate in dye degradation by direct oxidation [11, 22, 28].

$$\mathrm{ZnO} + h\upsilon \longrightarrow \mathrm{ZnO}\left(e^-_{sur} + h^+_{sur}\right) \quad (7)$$

$$h^+ + H_2O(OH^-) \longrightarrow OH^- \quad (8)$$

$$e^- + O_2 \longrightarrow O_2^- \quad (9)$$

The other authors also achieved the similar results in the nanohybrids of ZnO/CNC and ZnO/reduced graphene oxide (RGO) [29] (Table 3). It is noted that the photocatalytic activity of the ZnO/CNC-1.0 nanohybrid was higher than

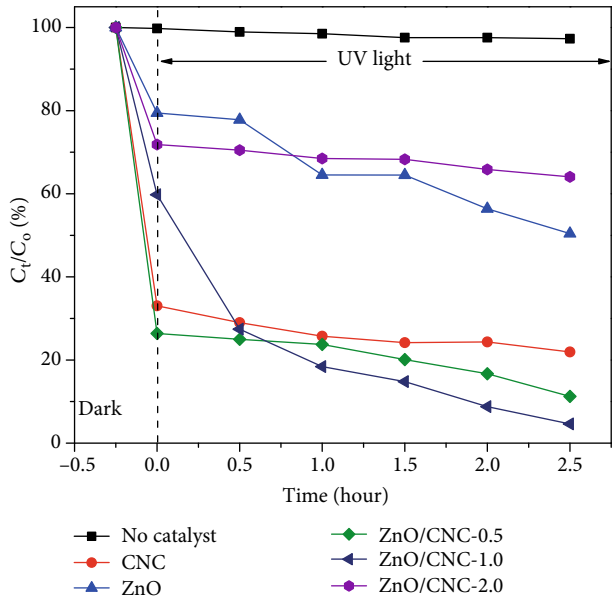

Figure 10: Photocatalytic and adsorption activity of ZnO and ZnO/CNC nanohybrids.

Table 3: The comparison of MB photocatalytic activity of the various ZnO/CNC nanohybrids.

Materials	The apparent first-order rate constant (min^{-1})	Ref.
ZnO/CNC-1.0	0.0157	This study
ZnO nanoparticles coated on nanocellulose from oil palm empty fruit bunches	0.0019	[22]
Sheet like(ZnO–CNC) nanohybrid synthesized by using hydrothermal method	0.016	[30]
Reduced graphene oxide–ZnO nanorod composites	0.039	[29]
ZnO/CNC synthesized by using hydrothermal method	0.028	[31]
ZnO–cellulose nanocomposite films from a cellulose–NaOH/urea/zincate solution	0.046	[32]

that for ZnO nanoparticles coated on nanocellulose from oil palm empty fruit bunches [22].

In resuming results of both photocalytic and adsorption activities, the higher photocatalytic ability of ZnO/CNC nanohybrids was obtained, the lower adsorption activity was observed.

4. Conclusions

Using a facile, one-step synthesis route, ZnO/CNC nanohybrids possessing high thermal stability were obtained. The ZnO nanocrystals of 50 nm dispersed quite homogeneously around the CNC due to the strong electrostatic interactions between Zn^{2+} ions and carboxyl groups of CNC. Moreover, the results also gave the evidence that the degradation of MB was contributed not only by the adsorption ability of CNC but also by the photocatalytic activity of ZnO. The competition between these two processes depends on the concentration ratio of zinc-precursor $Zn(NO_3)_2.6H_2O$ and CNC. The MB photodegradation of ZnO/CNC-1.0 was obtained as high as 95% during 150 min. Depending on the purpose of organic dye treatment, it was observed that the yield of adsorption and photocatalytic process could be controlled by changing the concentration ratio of zinc-precursor $Zn(NO_3)_2.6H_2O$ and CNC from 0.5 to 1.0. Such nanohybrids with improved properties show great potential for waste water treatment.

Data Availability

The data used to support the findings of this study are included within the article.

Conflicts of Interest

The authors declare that they have no conflicts of interest.

Acknowledgments

This research is funded by Vietnam National University Ho Chi Minh City (VNU-HCM) under grant number 562-2018-18-01.

References

[1] A. Dufresne, "Cellulose nanomaterial reinforced polymer nanocomposites," *Current Opinion in Colloid & Interface Science*, vol. 29, pp. 1–8, 2017.

[2] M. Fardioui, M. E. M. Mekhzoum, A. . K. Qaiss, and R. Bouhfid, "Bionanocomposite materials based on chitosan reinforced with nanocrystalline cellulose and organo-modified montmorillonite," in *Nanoclay Reinforced Polymer Composites: Nanocomposites and Bionanocomposites*, pp. 167–194, Springer, 2016.

[3] P. Dhar, D. Tarafder, A. Kumar, and V. Katiyar, "Effect of cellulose nanocrystal polymorphs on mechanical, barrier and thermal properties of poly (lactic acid) based bionanocomposites," *RSC Advances*, vol. 5, no. 74, pp. 60426–60440, 2015.

[4] D. Bagheriasl, P. J. Carreau, B. Riedl, and C. Dubois, "Enhanced properties of polylactide by incorporating cellulose nanocrystals," *Polymer Composites*, vol. 39, no. 8, pp. 2685–2694, 2018.

[5] L. Ma, Y. Zhang, and S. Wang, "Preparation and characterization of acrylonitrile-butadiene-styrene nanocomposites reinforced with cellulose nanocrystal via solution casting method," *Polymer Composites*, vol. 38, pp. E167–E173, 2017.

[6] D. Trache, M. H. Hussin, M. K. Haafiz, and V. K. Thakur, "Recent progress in cellulose nanocrystals: sources and production," *Nanoscale*, vol. 9, no. 5, pp. 1763–1786, 2017.

[7] C. Chen and L. Hu, "Nanocellulose toward advanced energy storage devices: structure and electrochemistry," *Accounts of Chemical Research*, vol. 51, no. 12, pp. 3154–3165, 2018.

[8] H. Voisin, L. Bergström, P. Liu, and A. Mathew, "Nanocellulose-based materials for water purification," *Nanomaterials*, vol. 7, no. 3, p. 57, 2017.

[9] Y.-Y. Li, B. Wang, M. G. Ma, and B. Wang, "Review of recent development on preparation, properties, and applications of cellulose-based functional materials," *International Journal of Polymer Science*, vol. 2018, Article ID 8973643, 18 pages, 2018.

[10] K. M. Lee, C. W. Lai, K. S. Ngai, and J. C. Juan, "Recent developments of zinc oxide based photocatalyst in water treatment technology: a review," *Water Research*, vol. 88, pp. 428–448, 2016.

[11] K. Qi, B. Cheng, J. Yu, and W. Ho, "Review on the improvement of the photocatalytic and antibacterial activities of ZnO," *Journal of Alloys and Compounds*, vol. 727, pp. 792–820, 2017.

[12] F. Awan, M. S. Islam, Y. Ma et al., "Cellulose nanocrystal–ZnO nanohybrids for controlling photocatalytic activity and UV protection in cosmetic formulation," *ACS Omega*, vol. 3, no. 10, pp. 12403–12411, 2018.

[13] F. Wu, "Copper and zin oxide composite nanostructures for solar energy harvesting," in *Engineering and Applied Science Theses and Dissertations*, Washington University, 2015.

[14] S. Singh, R. Pendurthi, M. Khanuja, S. S. Islam, S. Rajput, and S. M. Shivaprasad, "Copper-doped modified ZnO nanorods to tailor its light assisted charge transfer reactions exploited for photo-electrochemical and photo-catalytic application in environmental remediation," *Applied Physics A*, vol. 123, no. 3, p. 184, 2017.

[15] M. Samadi, M. Zirak, A. Naseri, E. Khorashadizade, and A. Z. Moshfegh, "Recent progress on doped ZnO nanostructures for visible-light photocatalysis," *Thin Solid Films*, vol. 605, pp. 2–19, 2016.

[16] P. R. Sharma, S. K. Sharma, R. Antoine, and B. S. Hsiao, "Efficient removal of arsenic using zinc oxide nanocrystal-decorated regenerated microfibrillated cellulose scaffolds," *ACS Sustainable Chemistry & Engineering*, vol. 7, no. 6, pp. 6140–6151, 2019.

[17] Y. Guan, H. Y. Yu, S. Y. H. Abdalkarim et al., "Green one-step synthesis of ZnO/cellulose nanocrystal hybrids with modulated morphologies and superfast absorption of cationic dyes," *International Journal of Biological Macromolecules*, vol. 132, pp. 51–62, 2019.

[18] M. Ul-Islam, W. A. Khattak, M. W. Ullah, S. Khan, and J. K. Park, "Synthesis of regenerated bacterial cellulose-zinc oxide nanocomposite films for biomedical applications," *Cellulose*, vol. 21, no. 1, pp. 433–447, 2014.

[19] W.-L. Zheng, W. L. Hu, S. Y. Chen, Y. Zheng, B. H. Zhou, and H. P. Wang, "High photocatalytic properties of zinc oxide nanoparticles with amidoximated bacterial cellulose nanofibers as templates," *Chinese Journal of Polymer Science*, vol. 32, no. 2, pp. 169–176, 2014.

[20] S. Azizi, M. Ahmad, M. Mahdavi, and S. Abdolmohammadi, "Preparation, characterization, and antimicrobial activities of zno nanoparticles/cellulose nanocrystal nanocomposites," *BioResources*, vol. 8, no. 2, p. 11, 2013.

[21] M. S. Jahan, A. Saeed, Z. He, and Y. Ni, "Jute as raw material for the preparation of microcrystalline cellulose," *Cellulose*, vol. 18, no. 2, pp. 451–459, 2011.

[22] K. Lefatshe, C. M. Muiva, and L. P. Kebaabetswe, "Extraction of nanocellulose and in-situ casting of ZnO/cellulose nanocomposite with enhanced photocatalytic and antibacterial activity," *Carbohydrate Polymers*, vol. 164, pp. 301–308, 2017.

[23] H.-Y. Yu, G. Y. Chen, Y. B. Wang, and J. M. Yao, "A facile one-pot route for preparing cellulose nanocrystal/zinc oxide nanohybrids with high antibacterial and photocatalytic activity," *Cellulose*, vol. 22, no. 1, pp. 261–273, 2015.

[24] M. Wada, L. Heux, and J. Sugiyama, "Polymorphism of cellulose I family: reinvestigation of cellulose IVI," *Biomacromolecules*, vol. 5, no. 4, pp. 1385–1391, 2004.

[25] S. Nam, A. D. French, B. D. Condon, and M. Concha, "Segal crystallinity index revisited by the simulation of X-ray diffraction patterns of cotton cellulose Iβ and cellulose II," *Carbohydrate Polymers*, vol. 135, pp. 1–9, 2016.

[26] B. K. Sharma, N. Khare, S. K. Dhawan, and H. C. Gupta, "Dielectric properties of nano ZnO-polyaniline composite in the microwave frequency range," *Journal of Alloys and Compounds*, vol. 477, no. 1-2, pp. 370–373, 2009.

[27] Q.-S. Liu, M. F. Zhu, W. H. Wu, and Z. Y. Qin, "Reducing the formation of six-membered ring ester during thermal degradation of biodegradable PHBV to enhance its thermal stability," *Polymer Degradation and Stability*, vol. 94, no. 1, pp. 18–24, 2009.

[28] A. Balcha, O. P. Yadav, and T. Dey, "Photocatalytic degradation of methylene blue dye by zinc oxide nanoparticles obtained from precipitation and sol-gel methods," *Environmental Science and Pollution Research*, vol. 23, no. 24, pp. 25485–25493, 2016.

[29] K. Huang, Y. H. Li, S. Lin et al., "A facile route to reduced graphene oxide-zinc oxide nanorod composites with enhanced photocatalytic activity," *Powder Technology*, vol. 257, pp. 113–119, 2014.

[30] S. Y. H. Abdalkarim, H. Y. Yu, C. Wang, L. X. Huang, and J. Yao, "Green synthesis of sheet-like cellulose nanocrystal–zinc oxide nanohybrids with multifunctional performance through one-step hydrothermal method," *Cellulose*, vol. 25, no. 11, pp. 6433–6446, 2018.

[31] G. Wei, H. F. Zuo, Y. R. Guo, and Q. J. Pan, "Synthesis of ZnO with enhanced photocatalytic activity: a novel approach using nanocellulose," *BioResources*, vol. 11, no. 3, pp. 6244–6253, 2016.

[32] F. Fu, J. Gu, X. Xu et al., "Interfacial assembly of ZnO–cellulose nanocomposite films via a solution process: a one-step biomimetic approach and excellent photocatalytic properties," *Cellulose*, vol. 24, no. 1, pp. 147–162, 2017.